Viscous Energy Dissipation in Frozen Cryogens

by

Steven J. Meitner

A thesis submitted in partial fulfillment of

the requirements for the degree of

Master of Science

(Mechanical Engineering)

at the

UNIVERSITY OF WISCONSIN – MADISON

2008

APPROVED

_____

Professor John Pfotenhauer

January 10, 2008

Abstract

ITER is an international research and development project with the goal of demonstrating the feasibility of fusion power. The fuel for the ITER plasma is injected in the form of frozen deuterium pellets; the current injector design includes a batch extruder, cooled by liquid helium. A more advanced fuel system will produce deuterium pellets continuously using a twin-screw extruder, cooled by a cryocooler. One of the critical design parameters for the advanced system is the friction associated with the shearing planes of the frozen deuterium in the extruder; the friction determines the required screw torque as well as the cryocooler heat load.

An experiment has been designed to measure the energy dissipation associated with shearing frozen deuterium. Deuterium gas is cooled to its freezing point in the gap between a stationary outer canister and a rotating inner cylinder. The dissipation is measured mechanically and through calorimetric means. The experiment has also been used to measure dissipation in other cryogens (e.g., hydrogen, neon, and deuterium) as a function of rotational velocity and temperature. This paper describes the design and construction of the experiment and presents measurements over a range of cryogens and test conditions.

Acknowledgements

I would like to express my gratitude to my advisors John Pfotenhauer and Gregory Nellis for their help in all areas of my education. I am grateful for the opportunities they have provided me, first starting as an undergraduate research assistant, continuing on through my graduate studies, and this research. The knowledge they contributed to my education is invaluable.

I would also like to thank Dan Hoch. Without his knowledge of cryogenic engineering, and his ability to teach experimental manufacturing processes, the experiment would have been immeasurably more difficult. I would like to thank Mark Andraschko for setting the experiment on a good path, making it easy for me to follow. Larry Baylor and Steve Combs from Oak Ridge National Laboratory have also provided support necessary for the success of the project.

Koua Moua and Mike Heiss have been extremely valuable undergraduate assistants. I am also grateful to everyone in both the cryogenics laboratory, and the solar energy laboratory. Gabe, Ed, Jim, Kris, Kurt, Ryan, Harrison and many others have made important contributions.

Finally, I would like to thank my mother and Cassandra. Without their patience and support, it would have been impossible to continue with my education. I cannot thank them enough.

Table of Contents

List of Figures

List of Tables

Chapter 1 Introduction

The world power production is dependent on a depleting source of fossil fuels. The combustion of coal and natural gas release over 13 billion metric tons of carbon-dioxide annually [1]. Carbon-dioxide is the major contributor in global warming and related effects. In response, countries such as France have increased their nuclear energy production, but have traded carbon-dioxide emissions for radioactive spent fuel waste. Renewable energies, such as wind power and solar power, are increasing in popularity, but due to energy storage issues, peaking plants are still required. In an attempt to solve these problems, energy research is being conducted to determine if a fusion reaction can be harness for energy production. Fusion would allow on-demand power production while having minimal radioactive waste.

1.1 ITER

ITER is an experimental reactor to be built in Cadarache France with the goal of harnessing a Deuterium-Tritium fusion reaction for future energy production. The ITER fusion research reactor is being designed by an international consortium that currently includes the United States, Russia, the European Union, Japan, China, Korea, and India. ITER is a tokamak design, in which the reactor confines a toroidal fusion plasma by strong magnetic fields, as shown in Figure 1.1.

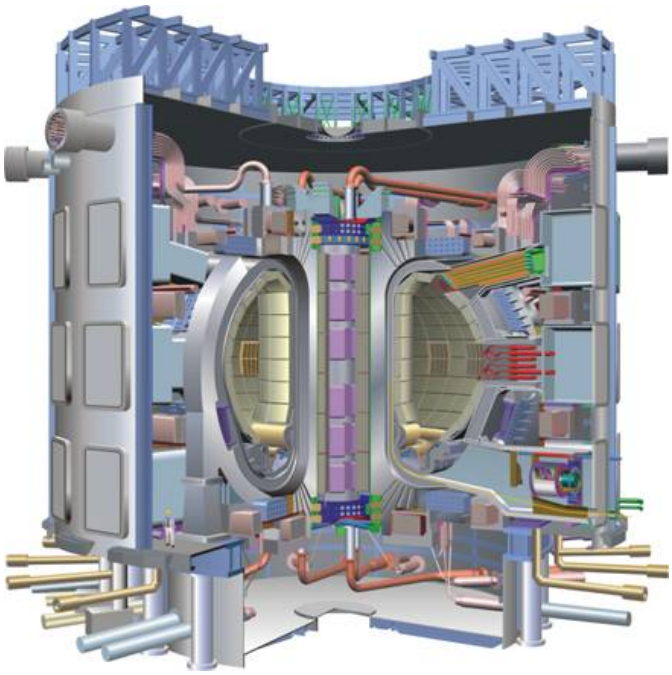

Figure 1.1 ITER Fusion Reactor Model [2]

1.2 Fusion Reaction

The reaction requires a great deal of energy to overcome the positive repulsive force of the protons, but once the nuclei come in contact with each other, strong nuclear forces combine them into a new nucleus. This reorganization, according to the chemical equation,

$$ {}_{1}^{2}H + {}_{1}^{3}H \rightarrow {}_{2}^{4}He + {}_{0}^{1}n + 17.6MeV \qquad (1.1) $$

results in a large release of energy. The isotopes combine in the contained plasma producing a heavier helium atom, and simultaneously releasing a neutron. The neutron is ejected from the plasma and its kinetic energy is collected.

A sustained reaction is required in order to overcome the initial reaction energy, and to collect the net energy for energy production. During the reaction, neutrons are ejected at

high speed from the plasma, but the heavier helium atoms slow and collide with other reactants. These collisions provide the plasma with thermal energy to maintain the reaction. Eventually, the helium will escape the plasma, so a continuous source of isotopes is needed to sustain the reaction.

1.3 Fuel Pellets

The reactants (fuel pellets) are introduced in the form of frozen cylinders approximately 6 mm diameter with a length to diameter ratio of one. The estimated fuel injection requirements for ITER are 3000 seconds of continuous pellet injection at a rate of up to 7 pellets per second [3]. The pellets are injected by a pressurized gas, through a guide tube, and into the plasma as shown in Figure1.2.

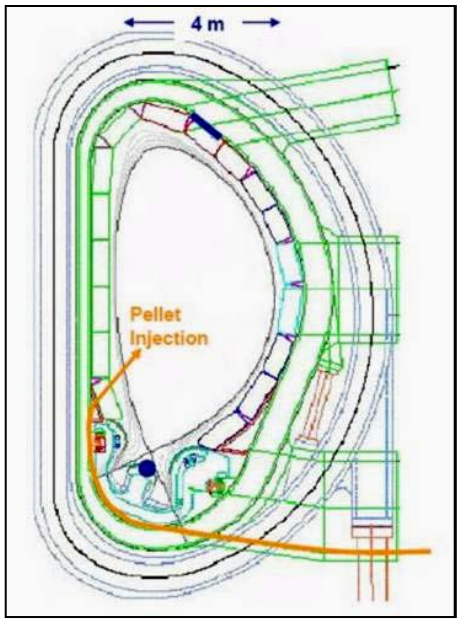

Figure 1.2 Tokomak Cross Section Detailing Fuel Pellet Injection Path [2]

The fuel pellets are produced in an extruder. Deuterium gas is introduced at one end of the extruder, chilled as it passes through the extruder, liquefied, solidified, and finally pushed out through the die. A punch cuts the extrudate into pellets before they are fired into the plasma.

1.4 Pellet Extruder Types

There are three types of extruders, the batch (or piston), single-screw, and twin-screw. The batch extruder, shown in Figure 1.3, pushes the extrudate through the die with a piston.

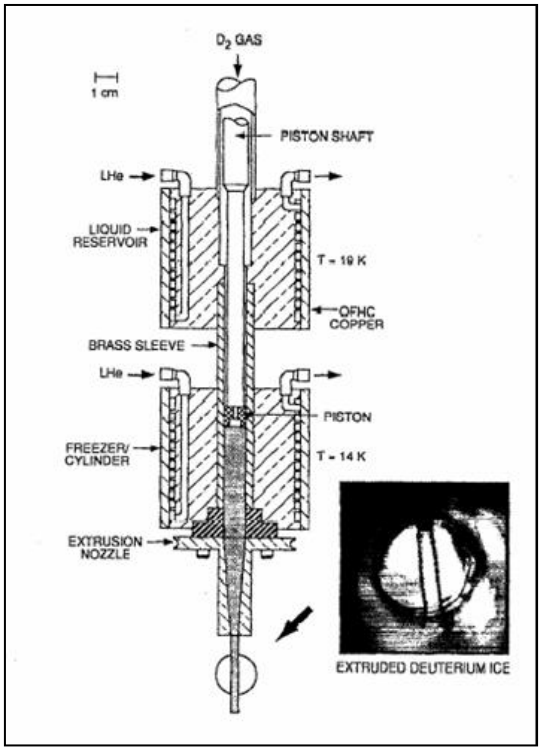

Figure 1.3 Batch Type Extruder [4]

After each “batch” is extruded, the piston is retracted to refill with new cryogen gas. The mass flow, and thus continuous pellet injection, must stop until the new cryogen gas can be frozen. The mass of the cryogen that can be contained in the extruder for a single batch is constrained by the shear strength of the cryogen. The piston shaft would yield if the shear stress was too great. The batch extruder does have the advantage of variable mass flow by changing the piston travel rate.

The single-screw extruder is shown in Figure 1.4.

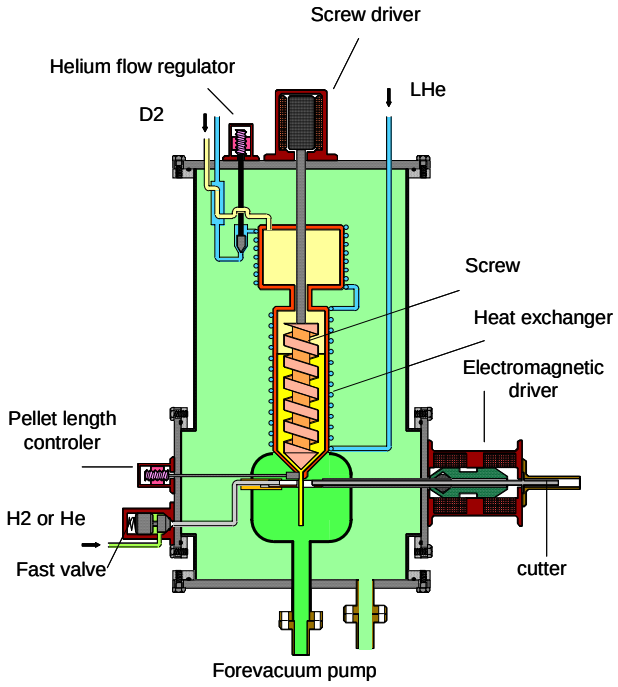

Figure 1.4 Single-Screw Type Extruder [5]

The single-screw extruder avoids the shortcoming of a batch operation by trapping the frozen cryogen in the screw flutes. As the screw is turned, the flutes push against the frozen cryogen to force it through the die. Since the entrance to the screw remains open,

a continuous supply of cryogen gas can be fed into the extruder to maintain constant mass flow.

The twin-screw extruder is shown in Figure 1.5.

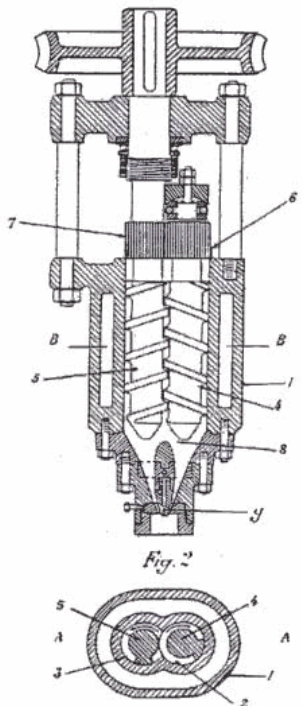

Figure 1.5 Twin-Screw Type Extruder[6]

A twin-screw extruder has been identified as the preferred configuration to produce the frozen deuterium. It combines both the advantages of continuous mass flow obtained with a single-screw extruder, and the positive mass displacement feature of a piston extruder. It avoids the disadvantage of the batch-mode operation associated with piston extruders and the reliance on wall friction to move the solid down through the die that comes with a single-screw extruder. In the twin-screw extruder, the interacting screws trap and displace the mass from one end to the other regardless of the viscous interaction with the wall. Mass flow can be adjusted by varying the screw rotation rates.

1.5 Extruder Design Parameters

Calculations associated with the twin screw extruder [7,8] investigate, among other issues, the amount of pressure required to push the mass through the extruder, and the amount of energy dissipated by the interaction between the mass and the internal extruder surfaces. For both issues, the results are dramatically different depending on whether a sheer strength associated with frozen solid or viscous forces associated with liquid-solid slush are assumed. The forces associated with the shearing planes of the frozen deuterium or the viscosity of deuterium slush will determine the required screw torque, as well as the amount of heat that is dissipated.

Typically, screw extruders are used to extrude plastic flows because the viscosity of the material decreases as temperature increases. In the cryogenic application the cryocooler must be able to remove the heat generated from viscous shear, or the extrusion will melt and become unstable.

One can conjecture that if the deuterium is solid and breaks under shear, it will yield a high initial torque until it shears, and then the torque will fall dramatically as a thin slip plane is developed. Furthermore, increasing the rotation rate after the slip plane has developed will have little effect on torque or heat load. If on the other hand, the deuterium behaves as a viscous slush, the starting torque will not be as substantial, and an increased rotation rate will result in an increased torque and heat load.

Chapter 2 Test Facility Design and Construction

An experiment comprised of the basic components shown in Figure 2.1, is used to determine the viscous or shear properties of frozen deuterium. The canister houses a solid cylinder of copper that rotates coaxial with the outer cylindrical wall of the canister. The main focus of the experiment is the annular space between the canister and inner cylinder, which is filled with deuterium gas. The deuterium gas is condensed, and then frozen, by cooling the annulus below the triple point of deuterium with a cryocooler.

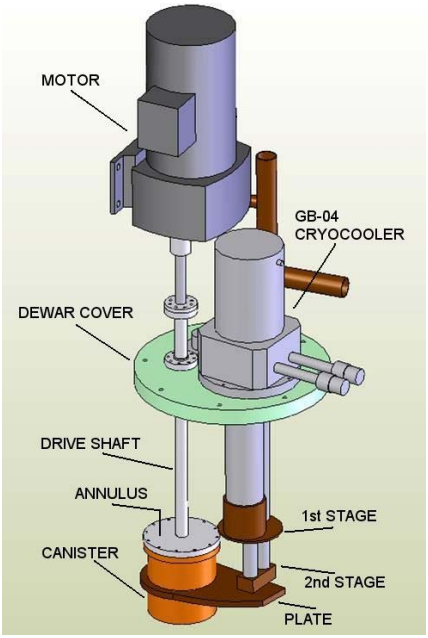

Figure 2.1 Schematic of the test apparatus

2.1 Dewar

The lower portion of the experiment is placed into a dewar that has an internal diameter and depth of 0.38 m and 1.0 m, respectively in order to provide a thermal barrier between

the cryo-cooled experiment against the warm ambient surroundings. The heat leak to the cold experiment is reduced by two methods. The first method reduces thermal radiation between the room temperature surroundings and the experiment by filling an annular jacket that surrounds the evacuated experiment space with liquid nitrogen. Thermal radiation from the room temperature is absorbed by the latent and sensible heat of the nitrogen. The 77 K boundary to which the experiment is subjected, results in a greatly reduced thermal radiation load. The evacuated experiment chamber provides the second method for reducing the heat load to the cold experiment in that the convective and conductive transfer that would otherwise occur across the gas is essentially eliminated.

2.1.1 Dewar Cover

The dewar cover is comprised of an upper cover and a lower adaptor ring. The upper cover is shown in Figure 2.2. The 305 mm diameter upper cover is a 25.4 mm thick disk of G10. The cover was sourced from a previous experiment in a smaller dewar. The cover was already machined with penetrations for the cryocooler feedthrough, electronic feedthrough, and vacuum port. The adaptor ring enabled the same the G10 cover to mount to the wider dewar used in this study. Three additional holes, two for the gas feedthroughs and one for the drive shaft, had to be drilled through the upper cover.

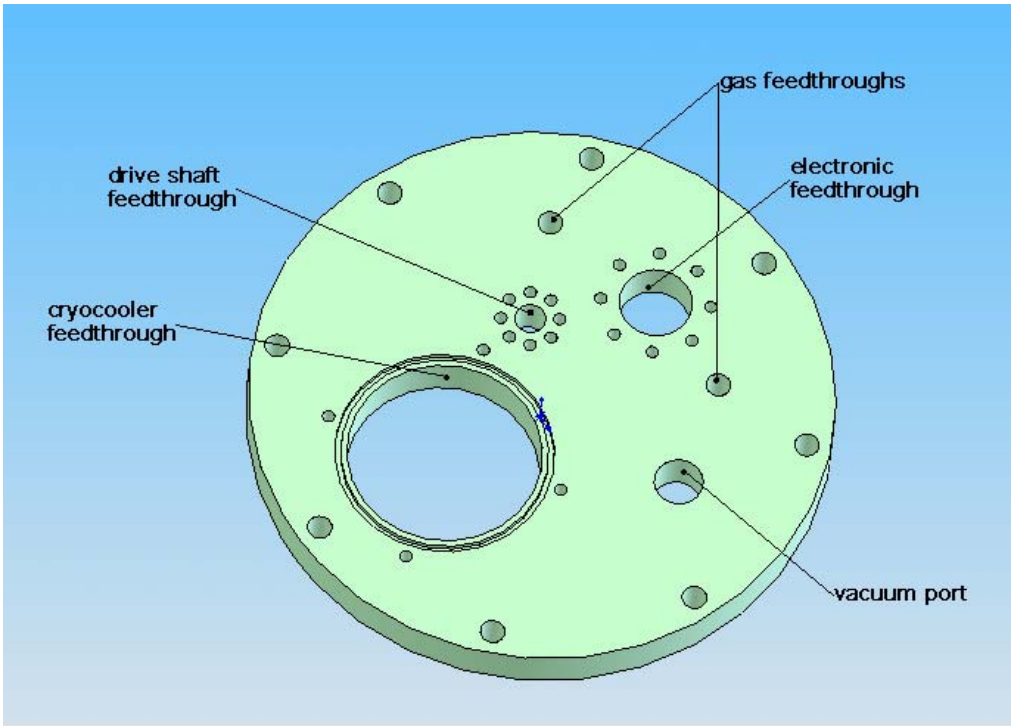

Figure 2.2 Upper dewar cover

The adaptor ring is shown in Figure 2.3. The 419 mm diameter adaptor ring is made from a 12.7 mm thick disk of 316 stainless steel. The disk required a 304.8 mm hole to be cut from the center to allow the experiment bolted to the upper cover to pass through. By comparing the time and tooling costs to machine the hole versus contracting out to a specialty shop, it was decided that outsourcing the cutting was more cost effective. Latitude Corporation [10] performed the cutting by an abrasive waterjet. The remaining machining was done in-house. Flats were machined to clear the nitrogen fill and vent ports on the dewar. The 1/4" -20 blind bolthole pattern that matches the pattern in the upper cover were drilled and tapped. Likewise, the 1/4" -20 through bolthole pattern that matches the dewar were drilled.

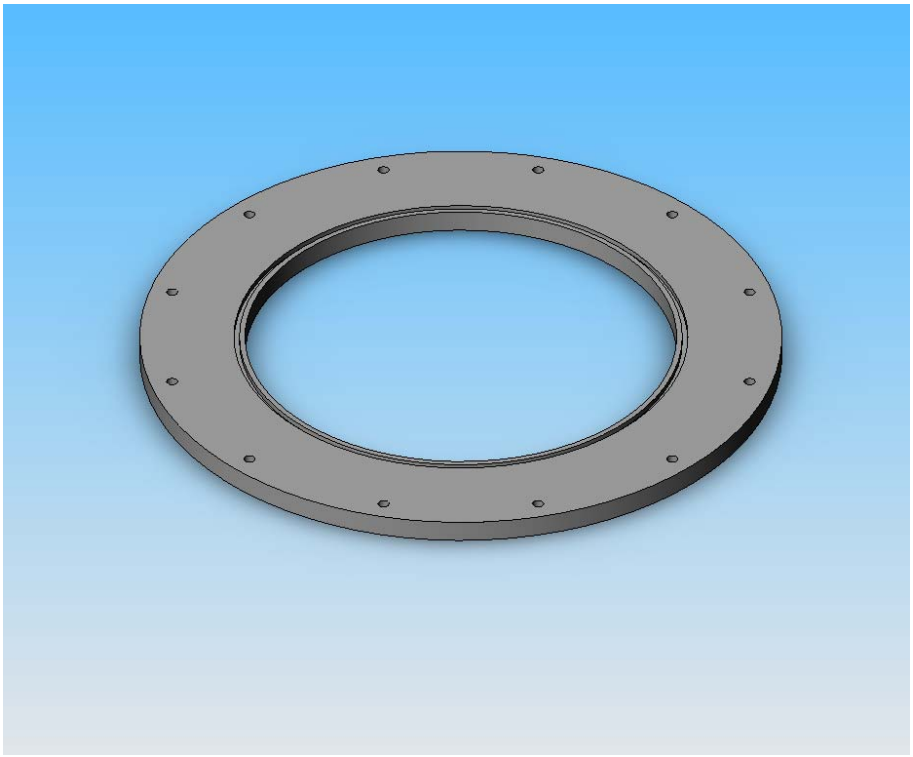

Figure 2.3 Lower adaptor ring

2.2 Annulus

The dimensions of the annulus are set to approximate planar shear between the inner cylinder and the outer canister. When operating the experiment, the inner cylinder is turned while the outer canister is held fixed shearing the cryogen. All machining of the annulus was completed in-house.

2.2.1 Inner Shear Cylinder

The inner structure of the annulus is created from a solid cylinder of oxygen free high conductivity (OFHC) copper, to facilitate a uniform temperature distribution. The cylinder has an outer diameter of 76.2 mm and a height of 101.6 mm.

2.2.2 Outer Shear Canister

The outer structure of the annulus is also constructed from a canister of OFHC copper. The canister has an inner diameter of 86.2 mm and a height of 102.4 mm. The height of the outer canister is slightly larger than the inner cylinder, allowing the inner cylinder to turn without contacting the top or bottom of the canister.

2.2.3 Ball Pivot

It is critical to keep the friction of the system as low as possible so that heating is caused primarily by the shearing of the deuterium. Friction between the cylinder and canister is reduced by the addition of a ball pivot. The 316 stainless steel ball pivot is machined from 12.7mm round stock. The ball was polished on a lathe with fine grit sandpapers and rubbing compound. The outer diameter of the ball pivot is 0.05mm larger than its press-fit hole machined into the bottom of the cylinder. The two parts were assembled by heating and expanding the copper while simultaneously chilling and contracting the ball pivot in liquid nitrogen. The ball pivot is then quickly removed from the nitrogen and press-fit into the cylinder. The ball pivot rests in a Kel-F cup in the bottom of the canister. The cup was pressed into the canister without heat. Kel-F was chosen for its high compression and impact strength and low coefficient of friction. The canister, cylinder, pivot, and pivot cup are shown in Figure 2.2.

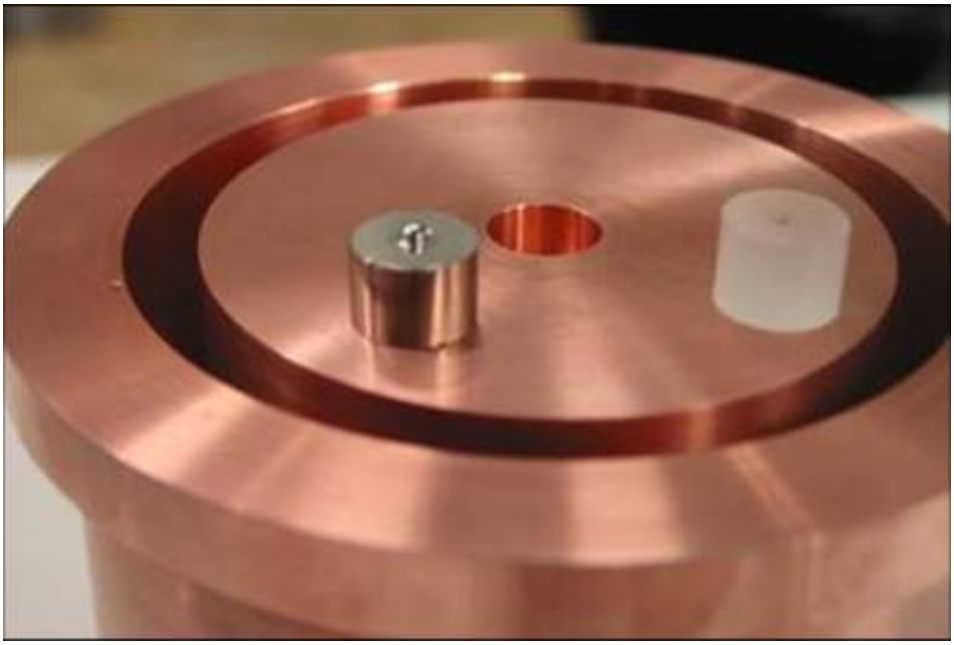

Figure 2.4 Annulus canister, cylinder, pivot, and pivot cup

2.2.4 Annulus Cover and Indium Seal

A 10 mm thick 316 stainless steel cover seals the annulus. The mating surface of the cover and canister were machined to create a tongue and groove seal. Rubber o-rings do not remain pliable at cryogenic temperatures, so an o-ring made from indium wire is used for the seal instead. As the cover bolts are tightened, the indium is extruded from the groove to create a hermetic seal. The groove is designed so that when the indium is compressed, it overfills the groove by 25%. The indium wire ends were cut diagonally from top to bottom and overlapped to create the ring as shown in Figure 2.4. The orientation is crucial to ensure that the indium is forced together when compressed. Prior to installation, the indium wire and mating surfaces were cleaned thoroughly with acetone.

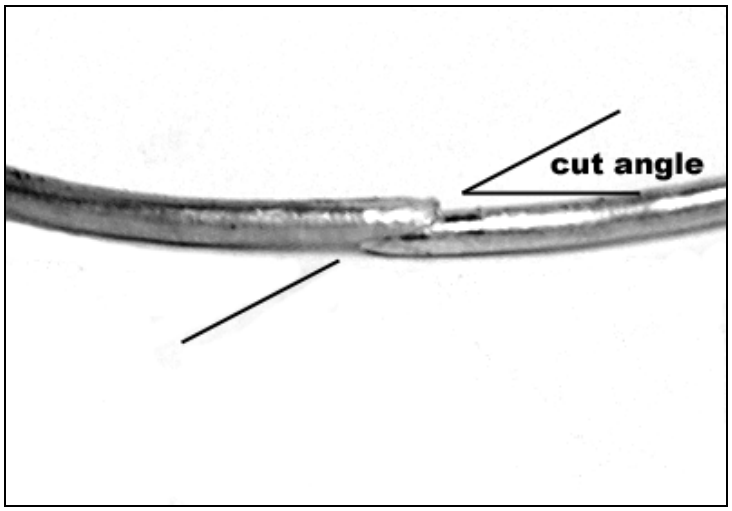

Figure 2.5 Indium wire overlap cut orientation

2.3 Drive Shaft

The inner rotating cylinder is connected to a drive shaft that extends up through the dewar cover. The drive shaft is sealed from the dewar vacuum space and the atmosphere by two outer tubes with o-ring flanges. The drive shaft dimensions, and those of the outer tube, are selected based on consideration of their shear strength and thermal conduction along their respective lengths. Specifically, the shaft and outer tube are designed to withstand the shearing and reaction torques, while simultaneously minimizing the conductive heat load on the cryocooler, as discussed in Chapter 2.6. The heat load to the cryocooler is dominated by the sum of conduction along both the driveshaft and the outer tube.

2.3.1 G10 Drive Shaft Design

A solid G10 rod was considered as an option for the drive shaft due to its relatively high shear strength and low conductivity; the maximum shear stress $(\tau_{\max})$ for G10 is 45 MPa [11] which is only 4-5x less than stainless steel.

The diameter of the G10 drive shaft (d_{G10}) that is required to handle the shaft torque (T_{shaft}) is calculated according to:

$$\tau_{\max G10} = \frac{T_{shaft}\ FS\left(\frac{d_{G10}}{2}\right)}{J_{G10}} \tag{2.1}$$

where FS is the factor of safety used in the design and J_{G10} is the polar moment of inertia of the G10 rod :

$$J_{G10} = \frac{\pi\left(\frac{d_{G10}}{2}\right)^4}{2} \tag{2.2}$$

The diameter of the G10 drive shaft that will handle the torque with no safety factor is 0.02261 m, (0.89 in); a common commercially available G10 rod with diameter of 0.0254 m, (1 in) will provide a safety factor of 1.5. Table 2.1 summarizes the parameters that were used for this calculation.

Table 2.1. Parameters and results of stress calculations to determine G10 design driveshaft diameter.

Parameter	Symbol	Value
G10 maximum shear stress	$\tau_{\max G10}$	45 Mpa
Shaft torque	T_{shaft}	94.91 N-m
Safety factor	FS	1.5
G10 rod polar moment of inertia	J_{G10}	4.086E-08 m^4
G10 rod diameter	d_{G10}	0.0254 m

Conduction through the drive shaft $\left(q_{G10}\right)$ is estimated according to:

$$q_{G10} = k_{G10} \frac{A_{G10}}{L_{shaft}} \left(T_H - T_C\right) \tag{2.3}$$

where k_{G10} is the integrated average conductivity of G10 [12], A_{G10} is the cross sectional area, L_{rod} is the rod length and T_H and T_C are the hot and cold end temperatures for the shaft. The calculated heat load through the G10 driveshaft is 0.27 W. Table 2.2 summarizes the parameters and results used in the heat load calculations.

Table 2.2. Summary of the heat transfer calculations through the G10 drive shaft design.

Parameter	Symbol	Value
Integrated average G10 conductivity	k_{G10}	0.7 W/m-K
G10 drive shaft cross section area	A_{G10}	5.067E-04 m^2
Length of the drive shaft	L_{shaft}	0.381 m
Dewar cover temperature	T_H	300 K
Canister cover temperature	T_C	10 K
Heat load through the drive shaft	q_{G10}	0.27 W

2.3.2 Outer Guide Tube Design

The outer diameter of the outer tube ($d_{OT,o}$) was chosen based on the selected size of the drive shaft; the selected value of $d_{OT,o}$ is 1.125 inch. The outer guide tube will be fabricated from 316 stainless steel because it can be easily welded to the o-ring sealing flanges on the dewar cover and the canister cover. Stainless steel 316 also has a high shear strength, 150 MPa [13]. The guide outer tube is meant to provide the reaction torque that holds the test facility stationary in the face of the shaft torque. Therefore, the thickness of the outer tube must be selected based on consideration of the stress induced by the shaft torque and the heat load through the outer tube must be computed.

The relationship between the torque and the shear stress induced in the hollow outer tube is:

$$\tau_{\max SS} = \frac{T_{shaft}\, FS \left(\frac{d_{OT,o}}{2} \right)}{J_{OT}} \tag{2.4}$$

where J_{OT} is:

$$J_{OT} = \frac{\pi}{2}\left[\left(\frac{d_{OT,o}}{2} \right)^2 - \left(\frac{d_{OT,o} - 2t_{OT}}{2} \right)^2 \right] \tag{2.5}$$

where t_{OT} is the wall thickness of the outer guide tube. The thinnest wall that can withstand the torque is 8.128E-04 m, (0.032 in). The closest commercially available wall thickness for the tube is 8.89E-04 m, (0.035 in). These tube dimensions provide 6.985E-04 m radial clearance between the inner surface of the outer tube and the driveshaft. Table 2.3 summarizes the parameters and results used in the stress calculation to determine the G10 design outer tube dimensions.

Table 2.3. Parameters and results of stress calculations to determine the outer tube dimensions.

Parameter	Symbol	Value
316 stainless steel maximum shear stress	$\tau_{\max SS}$	150 MPa
Shaft torque	T_{shaft}	94.91 N-m
Safety factor	FS	1.5
Outer tube polar moment of inertia	J_{OT}	1.483E-08 m^4
Outer tube outer diameter	$d_{OT,o}$	0.02858 m, (1.125 in)
Tube thickness	t_{OT}	8.89E-04 m, (0.035 in)

The rate of heat transfer through the outer guide tube is:

$$q_{OT} = k_{316} \frac{A_{OT}}{L_{shaft}} \left(T_H - T_C\right) \tag{2.6}$$

where A_{OT} is the cross-sectional area of the outer tube and k_{316} is the integrated average conductivity for 316 stainless steel [12]. The heat load conducted through the outer tube required for a G10 drive shaft is 1.00 [W]. Table 2.4 summarizes the parameters and results used in the heat load calculations.

Table 2.4. Parameters and results of calculations for the heat load through the G10 design outer tube.

Parameter	Symbol	Value
Integrated average 316 stainless steel conductivity	k_{316}	17 W/m-K
G10 design outer tube cross section area	A_{OT}	7.735E-05 m^2
Length of the outer tube	L_{OT}	0.381 m, (15 in)
Dewar cover temperature	T_H	300 K
Canister cover temperature	T_C	10 K
Heat load through the drive shaft	q_{OT}	1.00 W

The combined heat load due to conduction through the G10 driveshaft and 316 stainless steel outer tubing is 1.27 W. This is a relatively high heat load as compared to the load capacity of the cryocooler. Also, there are practical difficulties associated with connecting the G10 driveshaft to the motor and cylinder. The large heat load is related to the outer guide tube, which must be made large in order to confine the G10 drive shaft. The G10 drive shaft is large because it has a low strength compared to metals. Therefore, a possibly more attractive hollow stainless steel drive shaft alternative was also investigated.

This second design option uses a hollow 316 stainless steel driveshaft in place of the G10 rod. The conductivity of stainless is much greater than G10, but so is its maximum shear strength. Figure 2.6 shows that austenitic stainless steel has a thermal conductivity that is an order of magnitude greater than G10 throughout the temperature range of interest, from 10 K at the copper cylinder to 300 K at the dewar cover [12,14].

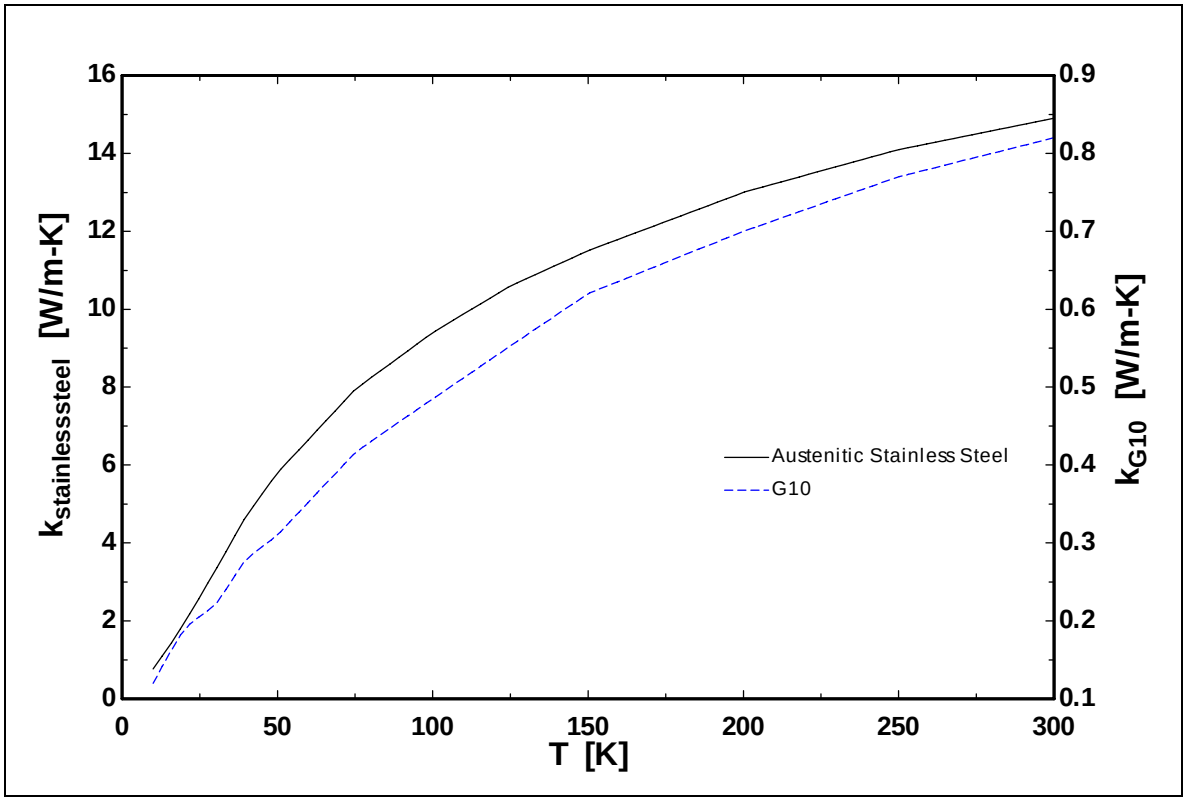

Figure 2.6 Thermal Conductivity of Austenitic Stainless Steel and G10

Even though the conductivity is much higher for stainless steel, the increased shear strength permits the use of a hollow tube of smaller diameter for the driveshaft. The outer guide tube diameter can also be reduced because of the smaller diameter driveshaft. If the combined cross sectional area of the driveshaft and outer tube is reduced by more than an order of magnitude, the heat load will be reduced.

The wall thickness of the drive shaft was specified as 8.89E-04 m, (0.035 in) for both driveshaft and outer guide tube due to the availability of this size. Shear stress and heat load calculations determine the hollow stainless steel driveshaft dimensions using the same equations provided in the previous sections.

Table 2.5. Parameters and results of stress calculations to determine stainless steel design dimensions.

Parameter	Symbol	Value
316 stainless steel maximum shear stress	$\tau_{\max SS}$	150 MPa
Stainless steel design driveshaft polar moment of inertia	J_{SS}	2.358E-09 m^4
Stainless steel design driveshaft outer diameter	d_{SSO}	0.01588 m, **(**0.625 in)
Stainless steel design driveshaft inner diameter	d_{SSI}	0.0141 m
Shaft torque	T_{shaft}	94.91 N-m
316 stainless steel conductivity	k_{316}	17 W/m-K
Stainless steel design driveshaft cross section area	A_{SS}	4.185E-05 m^2
Length of the driveshaft	L_{shaft}	0.381 m, (15 in)
Heat load through the drive shaft	q_{SS}	0.54 W
Stainless steel design outer tube cross section area	A_{SSOT}	5.072E-05 m^2
Heat load through the outer tube	q_{SSOT}	0.66 W

The combined heat load due to conduction for the stainless steel driveshaft and outer guide tube is 1.20 W. The heat loads are essentially the same for the two designs. Because the drive shaft could be easily welded to threaded couplers to mate with the motor and copper cylinder, the stainless steel design was chosen over the G-10 design. Figure 2.7 shows the completed driveshaft design based on stainless steel with the threaded inserts attached.

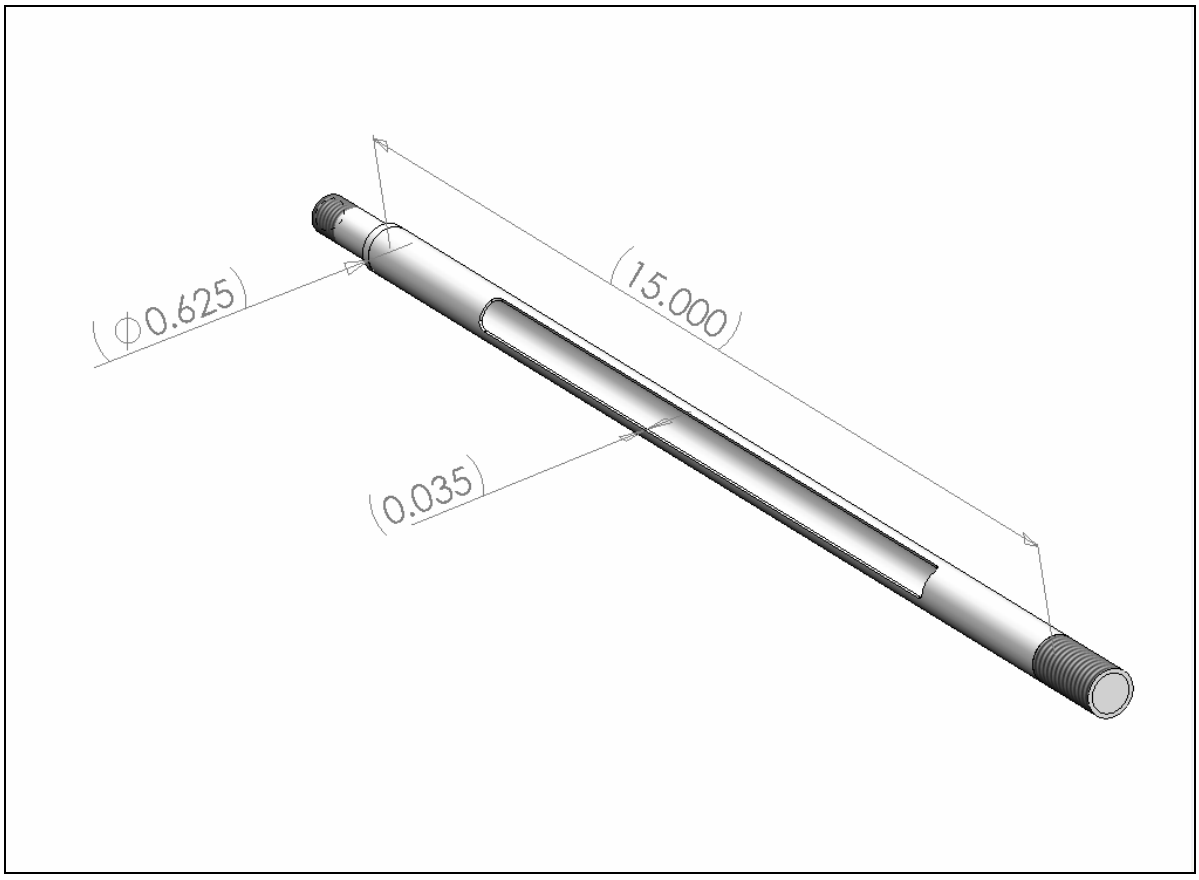

Figure 2.7 Stainless Steel Driveshaft with Threaded Couplers

2.3.3 Cylinder Coupling

The drive shaft is connected to the copper cylinder by a threaded coupler. The coupler was machined from 316 stainless steel round stock. One end of the coupler is attached to the cylinder by ¾" -16 NF thread. A shoulder is maintained at the base of the thread to allow the coupler to butt firmly against the cylinder, yet allow easy removal. Without the shoulder, the thread would bottom out and be extremely difficult to remove, if required.

The other end of the coupler is inserted and welded into the drive shaft. This was designed for ease of welding. The end of the solid round stock is bored, leaving a wall thickness of 5.08 mm so that the wall thickness of the coupler is comparable with that of

the drive shaft. Welding thin wall material requires similar wall thickness. If one wall is significantly thicker than the other, a large hole will be melted in the thin wall by the time the thick wall has enough heat input to fuse.

2.3.4 Motor Coupling

The drive shaft is connected to the motor by a threaded insert and a keyway coupler. The motor threaded insert is similar in design to the cylinder threaded insert, but smaller in diameter in order to fit through the o-ring flanges located on the inside of the drive-shaft guide tube.. The insert is made from a 3 inch long ½”-13 NC stainless steel bolt by removing the hex head and hollowing out the end for ease of welding to the drive shaft.

The remaining threaded portion of the bolt is left in its original form. It is threaded into the keyway coupler and held fixed with a jamb nut. The keyway coupler adapts the motor’s keyed shaft, to the threaded motor coupler. The keyway coupler is made from 1.25 x 2 inch 316 stainless steel round stock. A 0.75 inch shaft hole is concentrically bored for the motor shaft. A keyway is broached to match the motor keyway. A stainless ½”-13 NC nut is welded to the bottom of the coupler to match the bolt threads on the end of the drive shaft.

2.3.5 O-ring Flanges

The deuterium in the annulus is also able to flow into the gap between the outer guide tube and the drive shaft. The o-rings must seal the pressure experienced during boiling of the cryogen. A pressure relief valve ensures the maximum pressure does not exceed 22 [psig]. The outer tube and drive shaft need to be sealed to prevent deuterium leakage to

the vacuum space and atmosphere as shown in Figure 2.8. Three o-rings and four flanges are used to seal the annulus.

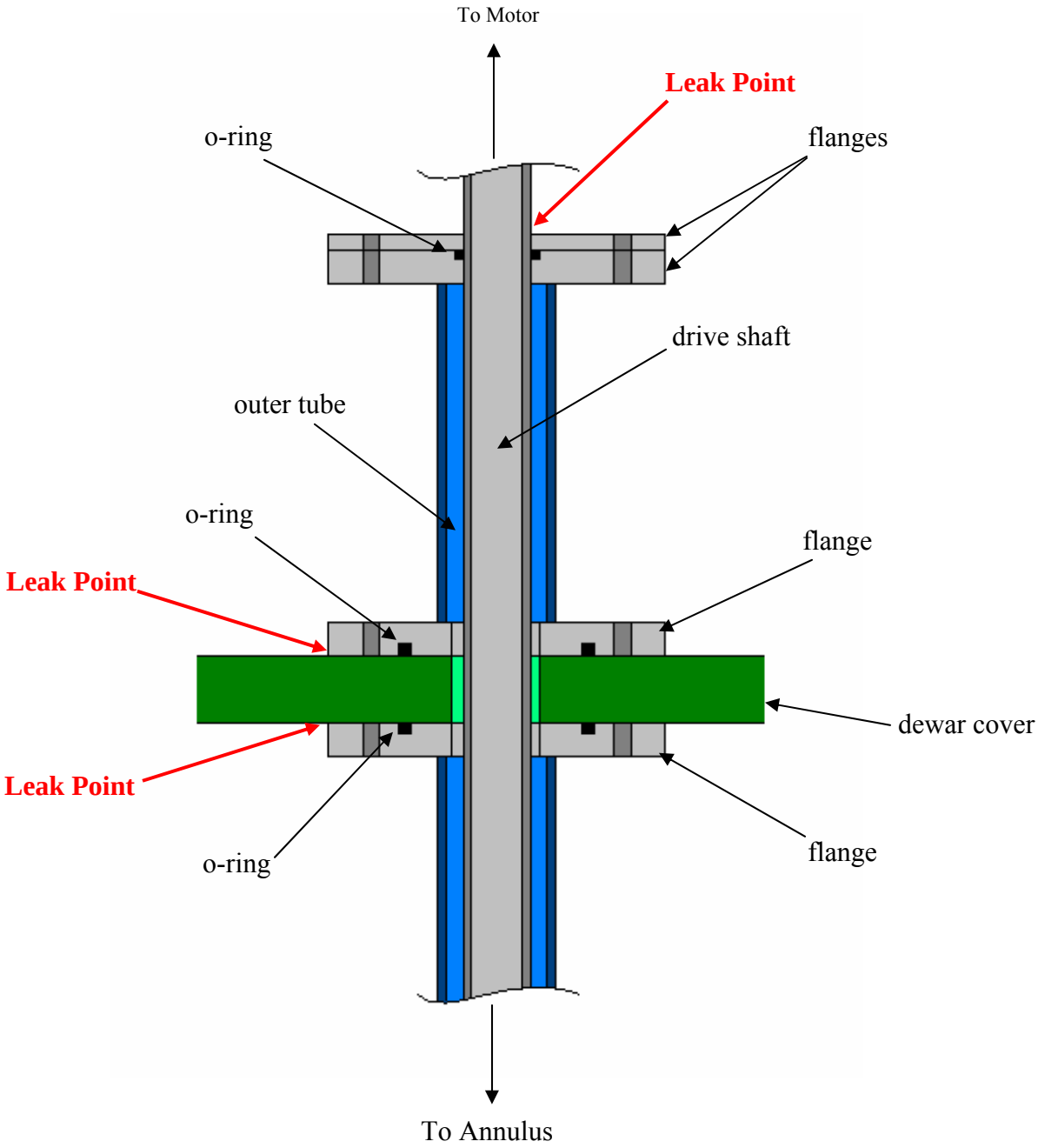

Figure 2.8 Annulus Sealing Locations

The lowest o-ring is a static seal compressed between the flange and the underside of the G10 dewar cover. It prevents the deuterium from leaking into the vacuum space. The o-ring flange design is shown in Figure 2.9.

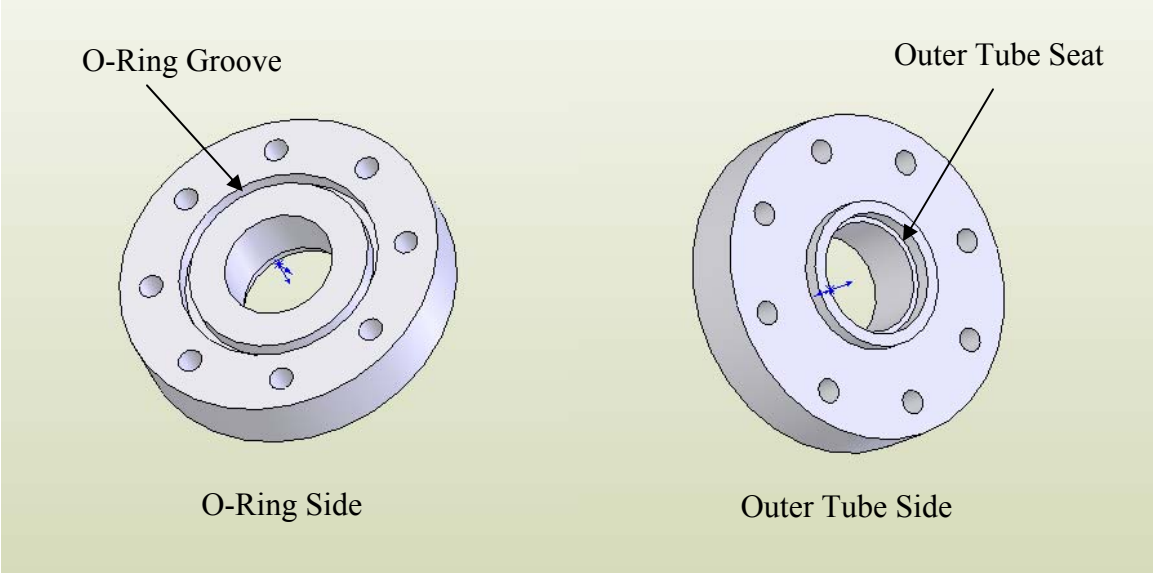

Figure 2.9 Static O-ring Flange

The flange is machined from a 9.525 mm thick piece of 50.8 mm diameter 316 stainless steel round stock. All machining was done in house on a lathe. A 17.27 mm through hole was concentrically bored to allow the drive shaft to pass through. The concentric o-ring groove was cut with a ThinBit® from Kaiser Tool. The dimensions of the o-ring groove are according to the Parker O-ring Handbook [15] for a static seal. The inside and outside diameters of the groove are 28.58 mm, and 31.75 mm respectively. The groove depth is 3.175 mm. A #12-32 through hole bolt pattern is drilled into the flange allowing it to bolt to a matching, threaded hole pattern on the bottom of the G10 dewar cover. Heli-coil® thread inserts are used in the holes on the dewar cover to provide enough strength so the threads do not strip as shown in Figure 2.10.

Figure 2.10 Heli-coil® thread inserts

The bottom of the flange is welded to the outer tube. A 7.62 mm seat is machined into the flange for the outer tube to press into. This aides in keeping the outer tube perpendicular with the dewar cover and maintaining alignment of the outer tube and drive shaft. The alignment is critical to ensure the drive shaft and outer tubes do not make contact, resulting in high system friction, and wear which will reduce the structural integrity of the tubes. The seat extends 2.5 mm out from the main flange at a wall thickness 2.5 mm. The extension provides a wall thickness of the same order of magnitude as the outer tube, which allows for easier welding with less heat distortion.

The o-ring above the dewar cover seals the deuterium from the atmosphere. The o-ring flange is identical to the flange underneath the dewar cover. Heli-coil® thread inserts are again used to strengthen the threads in the dewar cover. The hole pattern is shifted 22.5 degrees, so the upper and lower threaded hole patterns do not combine to create through holes which would allow a vacuum leak. A 127 mm section of outer tube is welded to the flange. It surrounds the drive shaft above the dewar cover, and extends up to the final o-ring seal.

The final seal at the top of the outer tube is a dynamic seal. The o-ring maintains contact with the drive shaft while it is turning and seals the deuterium from the atmosphere. The dynamic o-ring requires two flanges to create the seal as shown in Figure 2.11.

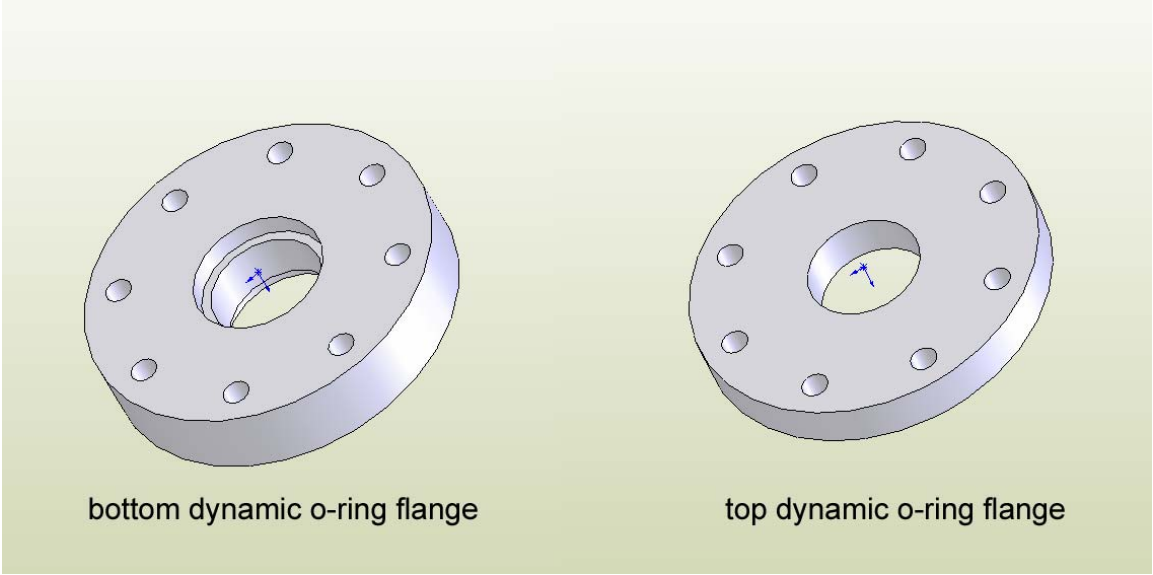

Figure 2.11 Dynamic O-ring Flanges

Like the dewar cover flanges, the dynamic seal flanges are made from 50.8 mm diameter 316 stainless steel round stock. The lower flange is welded to the outer tube and the upper flange is bolted on top of the lower flange. The lower flange has a seat to hold the

o-ring, and the upper flange is used to compress the o-ring against the driveshaft to create the seal.

The o-ring seat was machined using a boring bar on a lathe. The dimensions for the o-ring seat are from the Parker O-ring Handbook [15] for a dynamic seal. The outside diameter of the seat is 19.05 mm, and the depth is 3.175 mm. The holes that allow the drive shaft to pass through are 16.26 mm. The holes are smaller because the flanges must support the top and bottom of the o-ring where it contacts the drive shaft as shown in Figure 2.12. The bottom of the lower flange has an identical outer tube seat as the flanges used on the dewar cover.

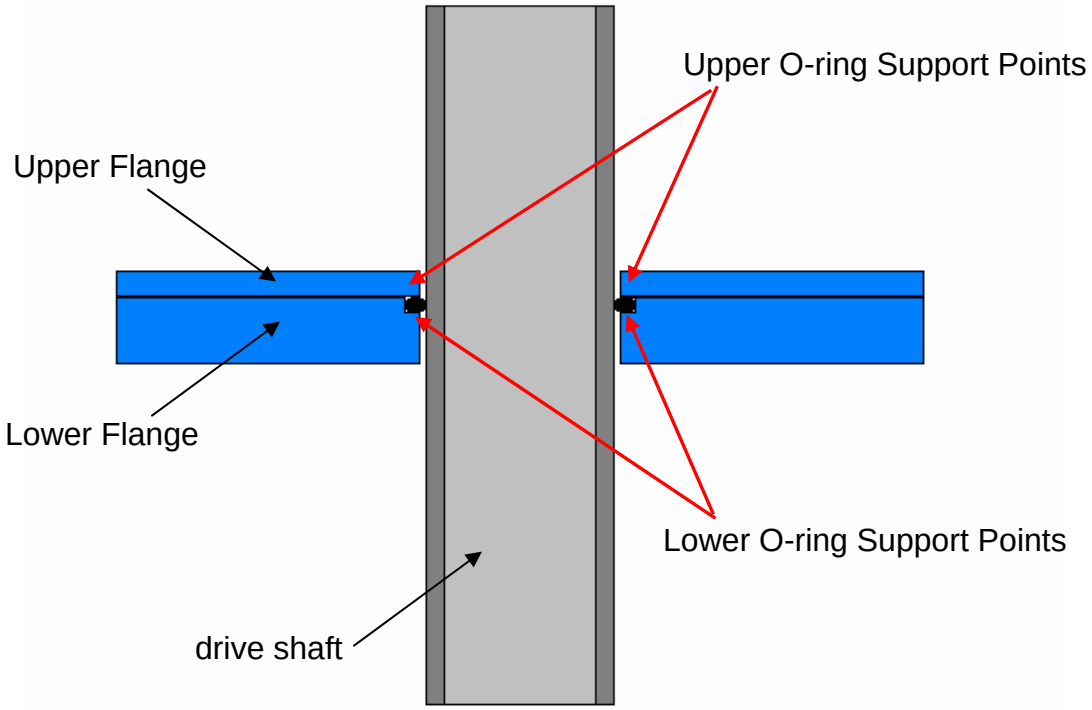

Figure 2.12 Dynamic O-ring Support Detail

2.4 Motor

The experimental tests require that the motor provide a consistent and high torque over a range of rotational speeds. The motor selection was based first on the requirement that the motor be able to provide a torque that is in excess of the shear torque estimation [7,8]. The motor specifications are listed in Table 2.6 and the motor is shown in Figure 2.13.

Table 2.6. Motor Specifications

Motor Specifications	
Brand	Leeson
Voltage	90V DC
Power	186.4 W, (1/4 hp)
Torque	122.7 N-m, (1087 in-lbf)
Speed	0 - 8 rpm
Gear Ratio	212:1
Shaft	19.05 mm, (3/4 in) keyed

Figure 2.13 Leeson DC Gear Motor

2.4.1 Speed Controller

An electronic speed controller is integrated with the motor. The speed controller allows the user to specify the speed, high speed limit, low speed limit, and acceleration. The controller uses an internal rectifier in order to provide the motor with the required 90 V DC from 120 V AC. The speed controller is shown in Figure 2.14.

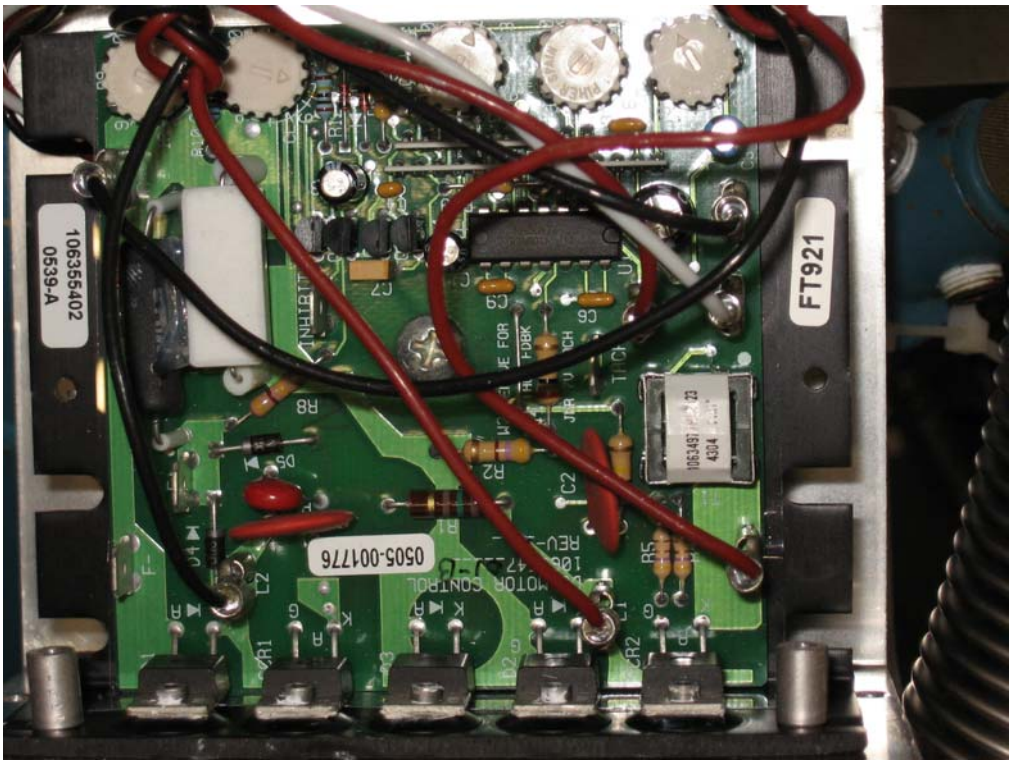

Figure 2.14 Motor Speed Controller

2.5 Safety Break Shear Pin

The shear force expected from the Deuterium can only be estimated and it is likely that there may be experimental conditions where the torque experienced by the motor is substantially larger than this nominal value. However, the thin walled drive shaft tube was optimized in order to limit the conduction heat load and therefore cannot tolerate a torque that is significantly in excess of the estimated nominal value without yielding and

damaging the apparatus. In order to protect the drive shaft tube from this type of failure, a shear pin is designed and installed in place of the standard steel motor shear pin; this shear pin provides a sort of mechanical fuse and is designed to yield before the drive shaft is damaged. The shear pin is shown in Figure 2.15. The shear pin is machined from a small piece of OFHC with a square cross-section (5.08 mm x 5.08 mm) that is 23.75 mm long. The length of the shear pin that contacts the motor and keyway coupler has been reduced to 12.7 mm so that it shears at a torque of 100 N-m.

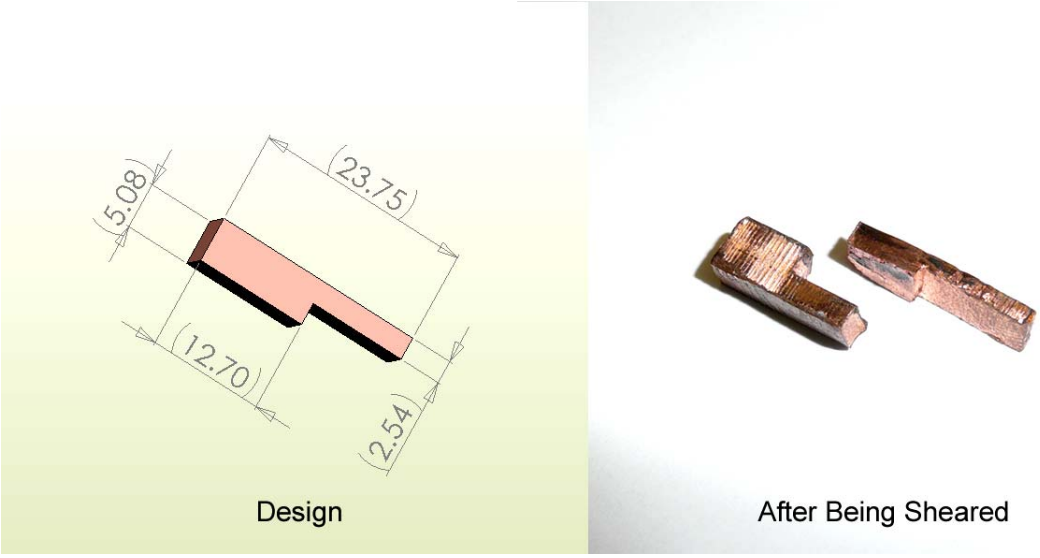

Figure 2.15 Safety Break Shear Pin

2.6 Cryocooler

The annulus is cooled by a Cryomech GB-04 two-stage cryocooler shown in Figure 2.16. The cryocooler is a Gifford-McMahon regenerative type refrigeration cycle.

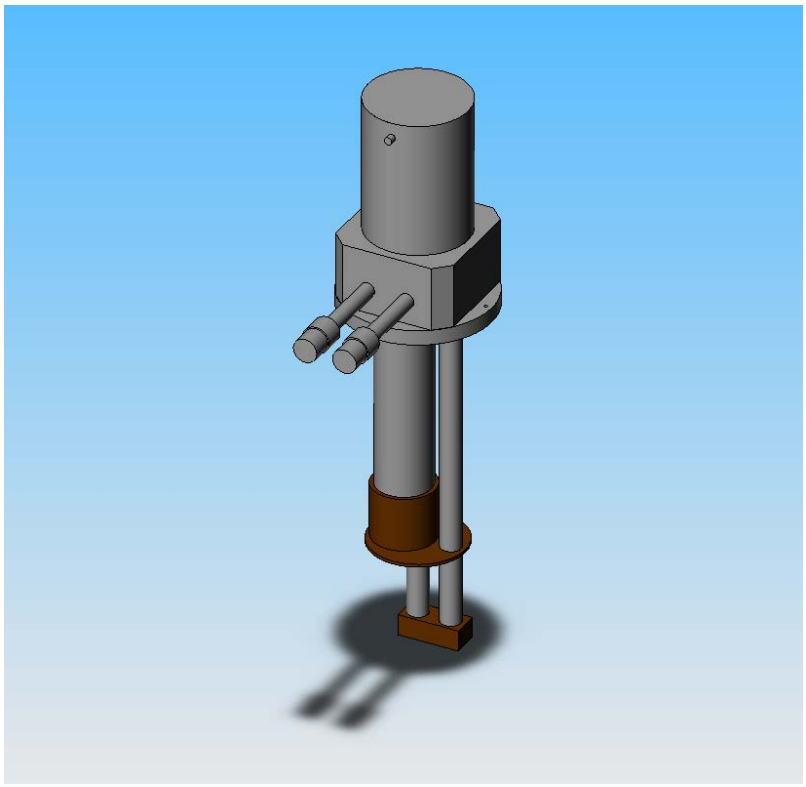

Figure 2.16 Cryomech GB-04 Cryocooler

A map of the cryocooler cooling capacity is provided by the manufacturer and shown in Figure 2.17; notice that the cryocooler provides about 3.5 watts of cooling power to the second stage at a load temperature of 10 K.

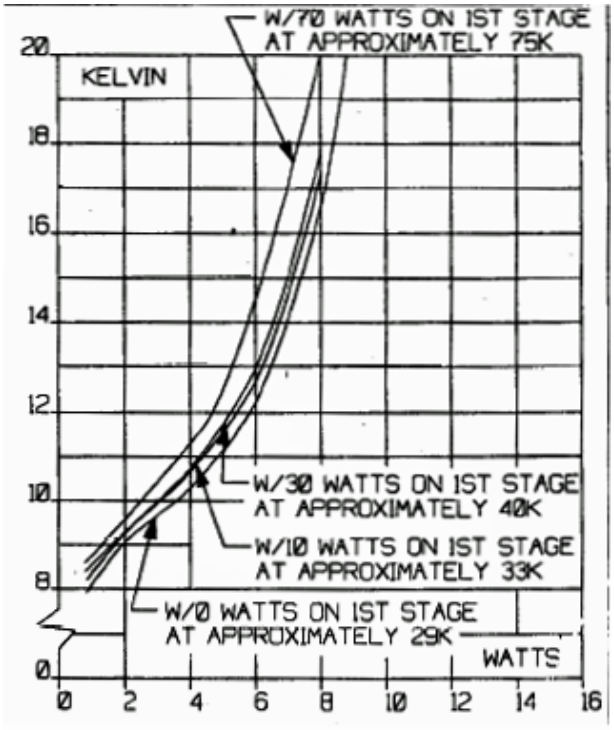

Figure 2.17 Cryomech GB-04 Cooling Capacity Map [16]

2.7 Thermal Connection Plate and Strap

The canister is brazed to a 9.53 mm thick OFHC plate that provides a thermal connection to the second stage of the cryocooler through a thermal strap that is installed between the OFHC connection plate and the cryocooler. The furnace braze joint between the OFHC plate and the canister was accomplished by Wisconsin Soldering and Brazing [17] using an inert gas furnace to prevent oxidation which would increase the thermal contact resistance that characterizes the joint. The filler material was chosen by Wisconsin Soldering and Brazing in order to closely match the thermal properties of copper. The rounded profile of the plate is dictated by the space constraints imposed by the dewar inner wall. The gap between the edge of the plate and the dewar wall is approximately 6 mm in order to allow adequate space for a multi-layer radiation shields to be installed. The plate is shown in Figure 2.18.

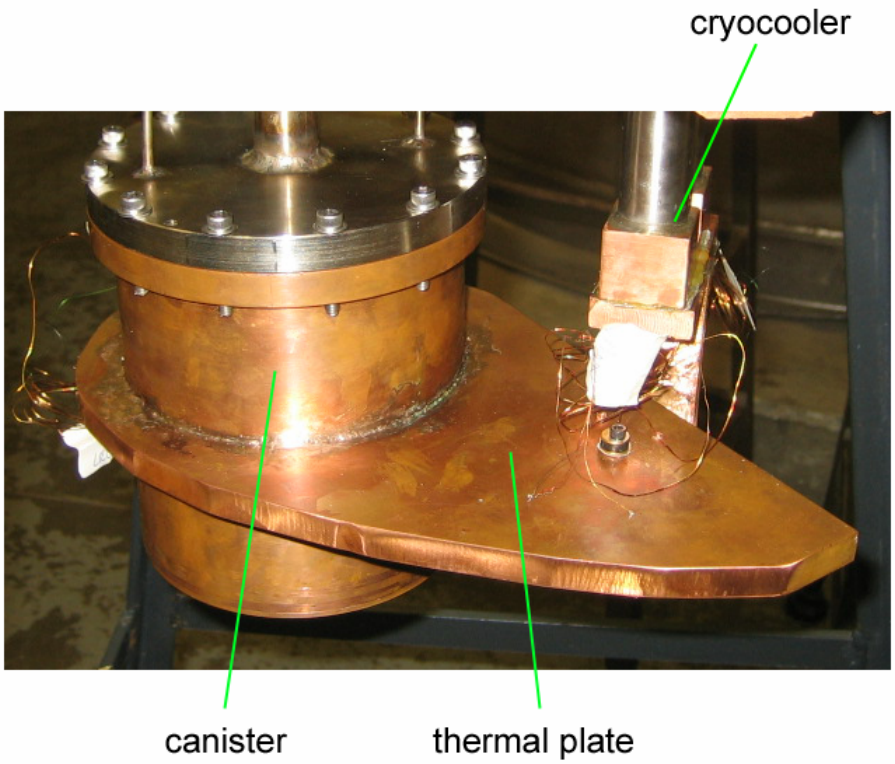

Figure 2.18 Thermal Connection Plate

The compliant thermal strap is fabricated from multiple, thin layers of copper. A rectangular OFHC adaptor block is sandwiched between the cryocooler and the thermal strap in order to offset the mounting point of the thermal strap so that it can be bended sufficiently to interface with the thermal plate. Indium foil, coated with a thin layer of Apiezon® N grease, is used to improve the thermal contact between the thermal strap, copper plate, adaptor plate and the cryocooler. The thermal strap and adaptor block are shown in Figure 2.19

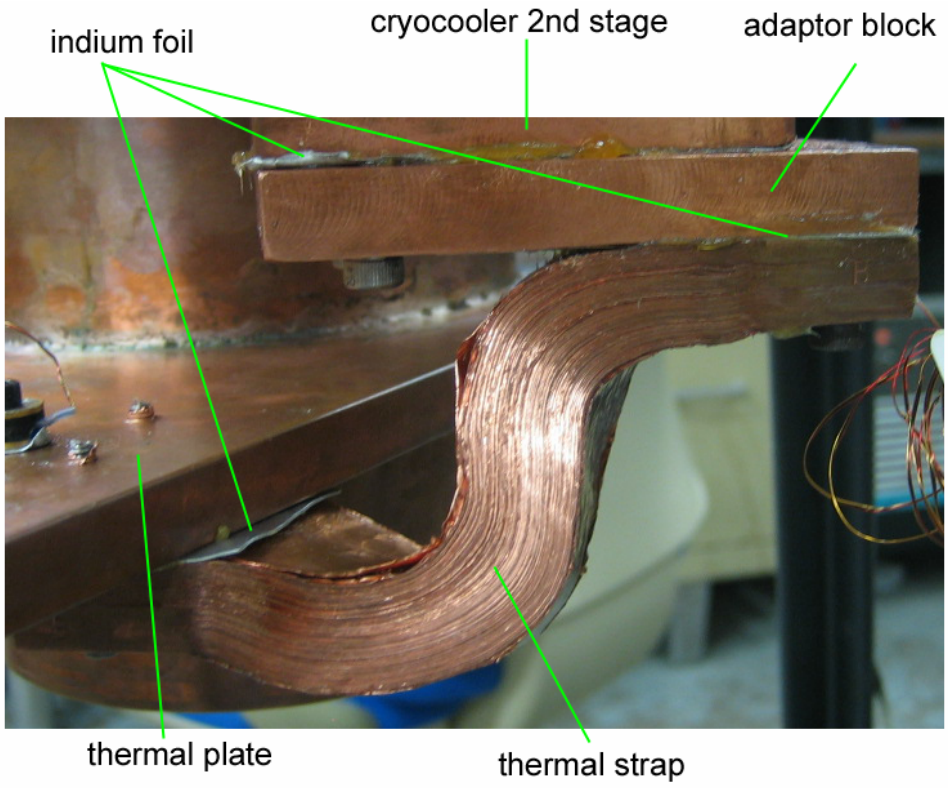

Figure 2.18 Thermal Connection Plate

The thermal strap maintains a conduction path, yet allows differential motion between the canister and the cryocooler; this differential motion may either be due to thermal contraction or from the reaction torque realized at the outer canister when the inner cylinder is turned. The outer tube will absorb the reaction torque and the resulting deflection in the outer tube $(deflect_{OT})$ is estimated according to

$$deflect_{OT} = \frac{T_{shaft}\ L_{shaft}}{J_{OT}\ G_{ss}} \tag{2.7}$$

where T_{shaft} is the shaft torque, L_{shaft} is the shaft length, J_{OT} is the polar moment of inertia of the shaft, and G_{ss} is the modulus of rigidity for 316 stainless steel [13]; nominal values for these parameters are summarized in Table 2.7.

Table 2.7. Parameters and results of calculations for drive shaft deflection.

Parameter	Symbol	Value
Shaft torque	T_{shaft}	94.91 N-m
Length of the driveshaft	L_{shaft}	0.381 m, (15 in)
Stainless steel design driveshaft polar moment of inertia	J_{OT}	4.192E-09 m^4
316 Stainless Steel modulus of rigidity	G_{ss}	75 GPa
Drive shaft deflection in radians	$deflect_{OT}$	0.247 rad
Drive shaft deflection in degrees	$deflect_{OT,\deg}$	7.964 deg

The estimated deflection of the driveshaft is about 8 degrees of rotation which is well within the capability of the compliant strap to absorb without exerting a substantial torque on the cryocooler. Without the flexible connection, strains imposed on the cryocooler could potentially cause the internal displacer to rub or seize thereby degrading or eliminating its cooling power.

2.8 Radiation Shield

A radiation shield surrounds the canister thereby intercepting the radiation heat load from the dewar wall (≈ 77 K), and cover (≈ 295 K). The shield is made from 1.588 mm thick copper sheet, and is thermally anchored to the first stage of the cryocooler. Additional radiation shielding from the dewar cover is provided by layers of MLI on the top of the copper radiation shield. The radiation shield and MLI blanket is shown in Figure 2.19.

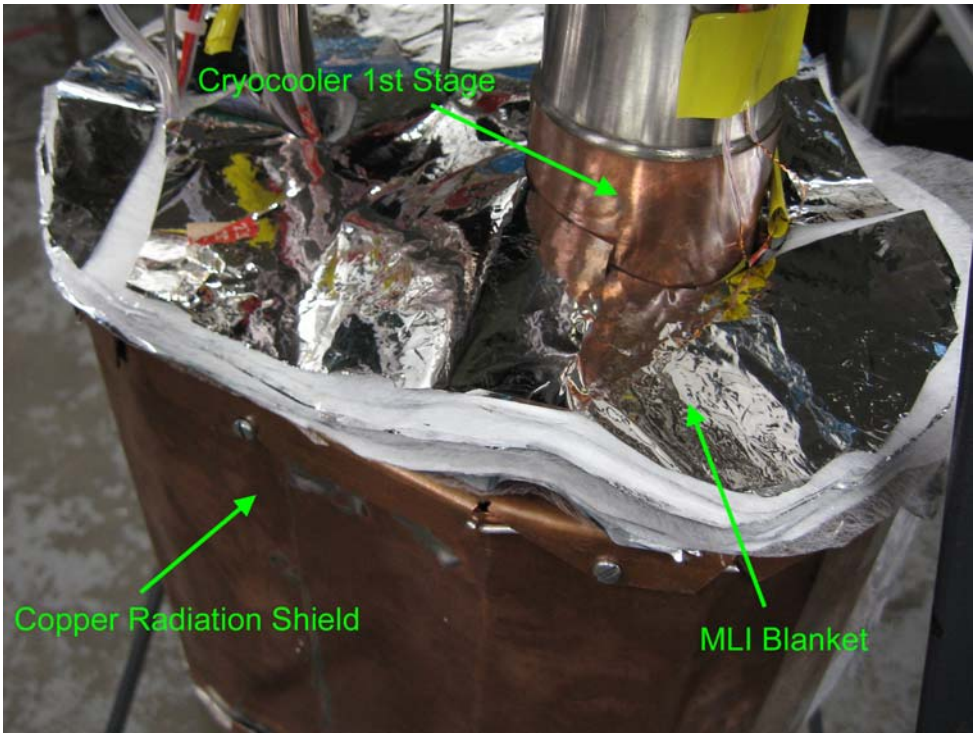

Figure 2.19 Radiation Shield and MLI Blanket

A skirt made from layers of MLI was taped to the side of the copper radiation shield to intercept radiation heat load from the dewar wall. Space constraints did not permit the MLI skirt to extend around the complete perimeter of the radiation shield. The skirt is shown in figure 2.20.

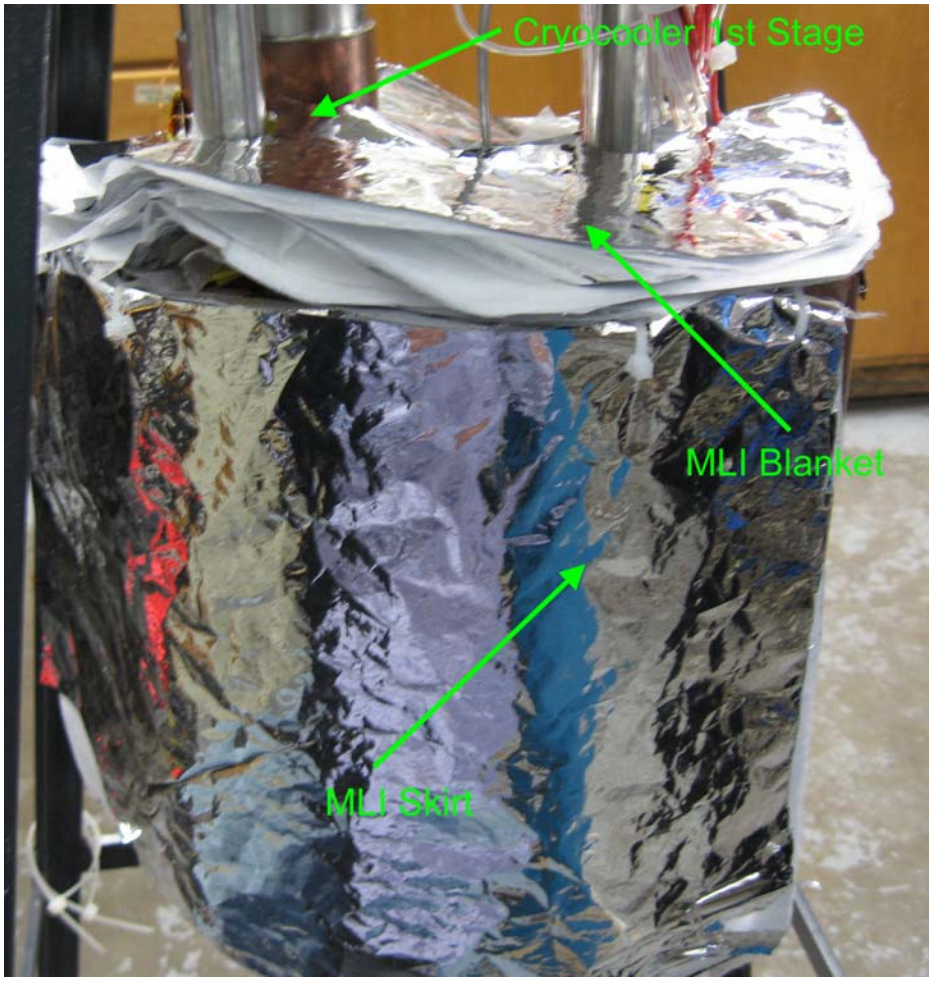

Figure 2.20 MLI Radiation Skirt

2.9 Fill Tubes

The annulus is filled with the cryogen from the supply cylinder through a system of tubing, an evacuation path and a fill path, as shown in figure 2.21.

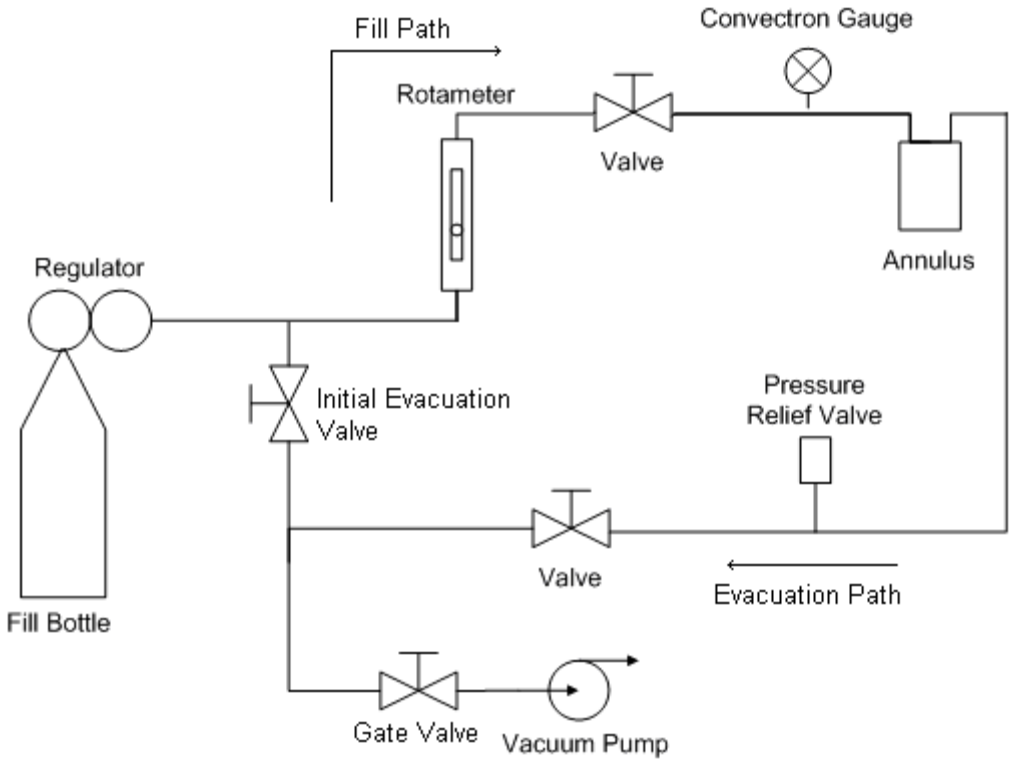

Figure 2.21 Cryogen Gas Flow Map

The annulus cover has two 3.175[mm] OD with 0.889 [mm] wall thickness stainless steel tubes welded to the top that extend up 76.2[mm] from the cover. The tubing is deliberately chosen to be a small diameter and thin wall to prevent heat leak to the annulus. The tubes terminate in 1/8" Swagelok® VCR female fittings.

The female fittings mate with male fittings that are welded to extension tubes, which extend up to the bottom of the G10 dewar cover. An "S" bend is made in the extension tubing to allow differential movement between the tubes and the drive shaft if they experience differing thermal contraction. The extension tubes and fittings are shown in Figure 2.22.

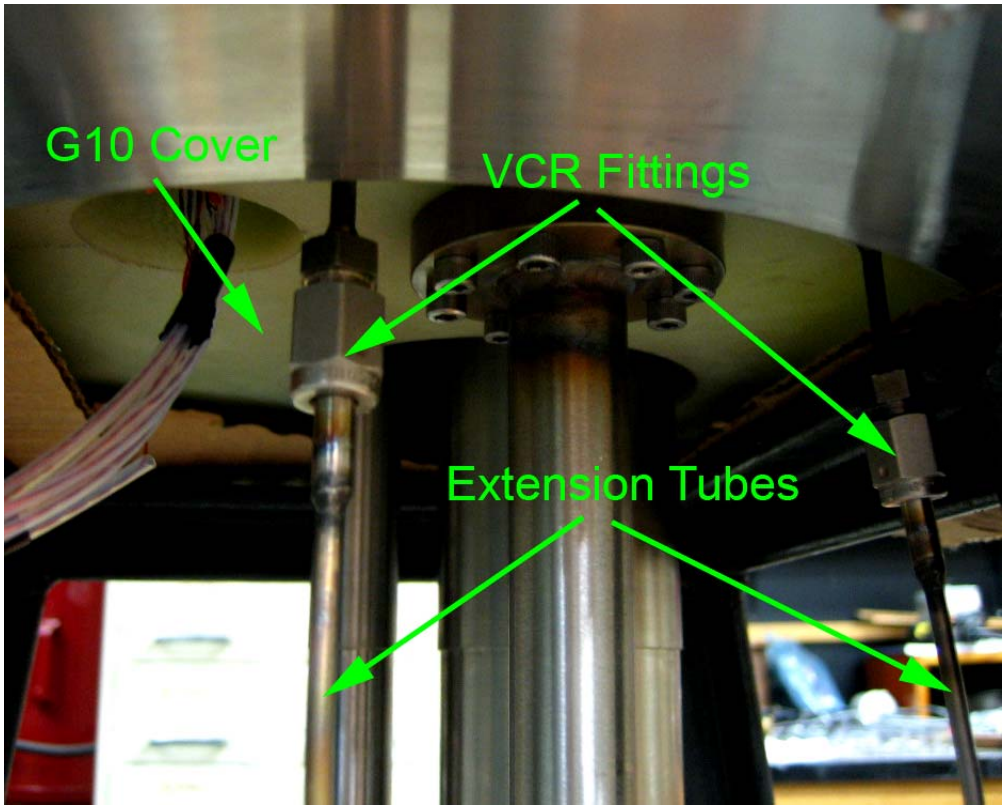

Figure 2.22 Fill Line Extensions and VCR Fittings

The sections extending through the G10 cover are made from 1/8" Swagelok® VCR – 1/4" NPT adaptor fittings. Short sections of 3.175[mm] stainless tubing are welded into the center of the 1/4" NPT side of the adaptor fittings. The G10 cover is drilled and tapped to accept the 1/4" NPT threads. The tubing and adaptor assemblies are then passed through the G10 cover. The NPT threads are coated with Stycast epoxy and the threads are tightened, making a hermetic seal. Above the G10 cover, the 1/4" VCR fittings are connected to 127 [mm] - long sections of stainless tubing that terminate in Swagelok® compression tube fittings. At this point, the function of the two lines differ. One path is used to evacuate the annulus, and the other is used to fill the annulus during

purging, as discussed in Chapter 4. A valve between the evacuation path and the fill path, is opened during the evacuation procedure to increase the speed of evacuation.

The evacuation path extends up from the G10 cover to a 22 psig pressure relief valve (shown in Figure 2.23) that prevents over pressurization that would otherwise result when the liquid cryogen in the annulus boils.

Figure 2.23 22 psig Pressure Relief Valve

An additional valve, between the pressure relief valve and the vacuum pump, along with the valve between the rotameter and the convectron gauge, enables modifications to the plumbing in the vicinity of the supply cylinder to be accomplished without disturbing the cryogen in the annulus. A Convectron vacuum gauge installed along the fill line is used to monitor the evacuation pressure in the annulus during purging, while a Dwyer rotameter is used as an indicator of cryogen gas flow into the annulus during the cool down process. The rotameter serves as a visual indicator that the fill line has not become

blocked with, for example frozen air or moisture during the cool down. The rotameter indicates flow in standard cubic feet per hour of air (SCFH), shown in Figure 2.24.

Figure 2.24 Rotameter Used as a Fill Monitor

Therefore, due to the differences in density of the cryogens to air, the gage has to be converted for each cryogen. An example of the conversion calculation is shown in Appendix A. After the rotameter, the fill path leads to the pressure fill gage and tank regulator.

Chapter 3 Measurement Systems

Energy dissipation by the shearing of the cryogen is measured and compared by both caloric and mechanical methods. The calorimetric method correlates energy dissipation to a power calculated from a measured temperature profile near the annulus. The mechanical method correlates energy dissipation with a power calculated from torque and rotation rates.

3.1 Calorimetric Measurement System

The caloric measurement devices are comprised of three Cernox® temperature sensors, a silicon diode temperature sensor, and an electric resistance heater. All temperature sensors are purchased from Lake Shore Cryotronics, Inc. The Cernox® temperature sensors (labeled T1, T2, T3) are mounted on the cryocooler second stage adaptor plate (T1), the thermal plate at the thermal strap attachment (T2), and on the upper back side of the canister, furthest from the cryocooler (T3). The silicon diode temperature sensor (T4) is mounted on the radiation shield that is attached to the cryocooler first stage. These temperature sensor mounting locations are illustrated in Figure 3.1.

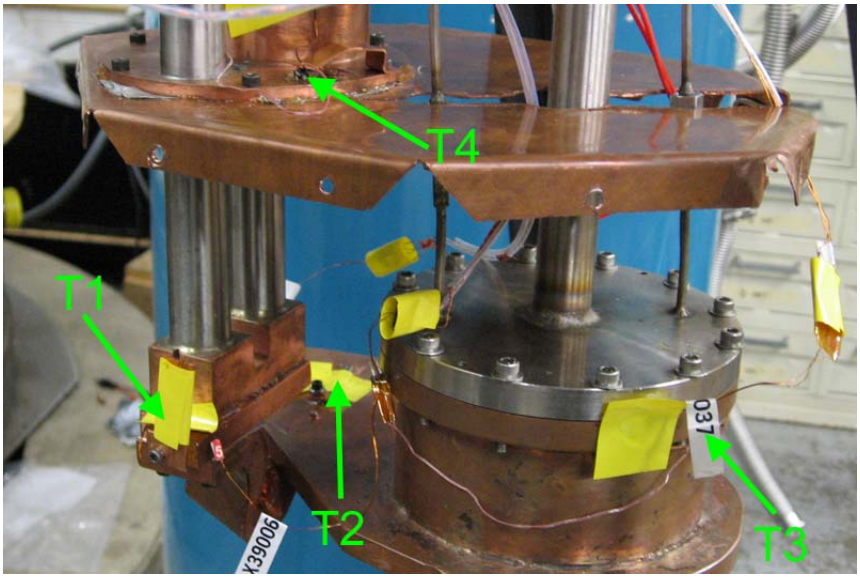

Figure 3.1 Temperature Sensor Locations

3.1.1 Cernox® Mounting

The Cernox® sensors T1 and T2 are bare chip package type CX-SD shown in Figure 3.2, and their dimensions are shown in Figure 3.3.

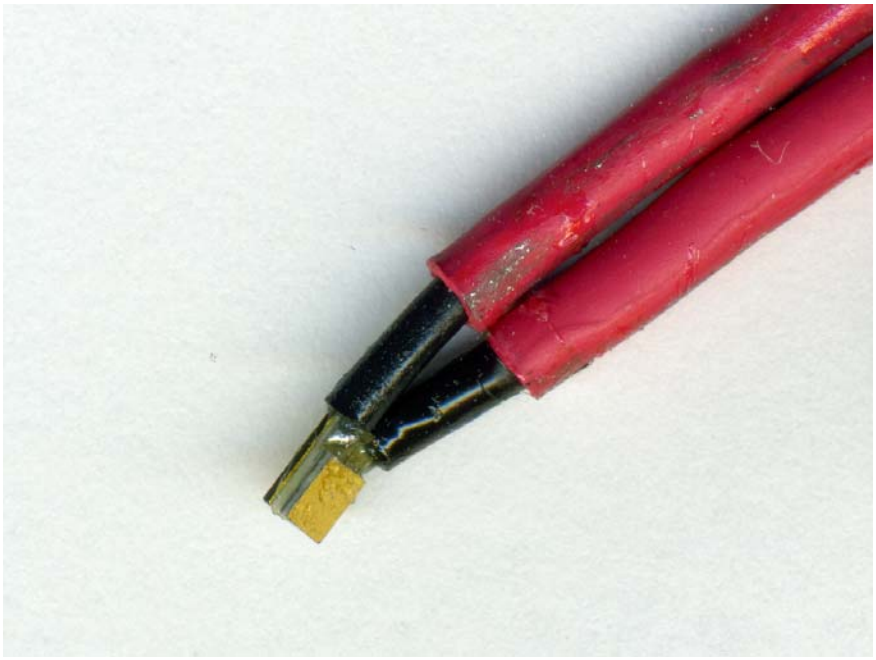

Figure 3.2 CX-SD Package Cernox®

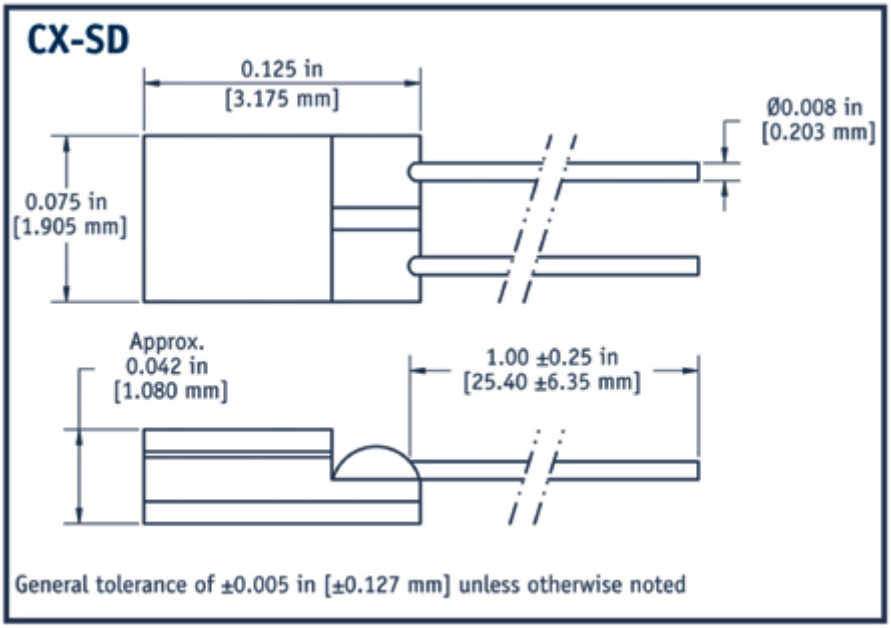

Figure 3.3 Cernox® CX-SD Dimensions [18]

The bare chip sensor requires electrical insulation from its surroundings but the chip must be placed in good thermal contact with the mounting location. Two mounting fixtures have been designed for this purpose, as shown in Figure 3.4. These mounting fixtures hold the sensor T1 against the adaptor plate and the sensor T2 against the thermal plate by capturing the chips inside a machined pocket. The adaptor and thermal plates mate with the pocket openings in order to create a cavity where the chips are inserted. The mounts are machined from OFHC and are attached with a #6x32 screw. The machined mount is shown in Figure 3.5.

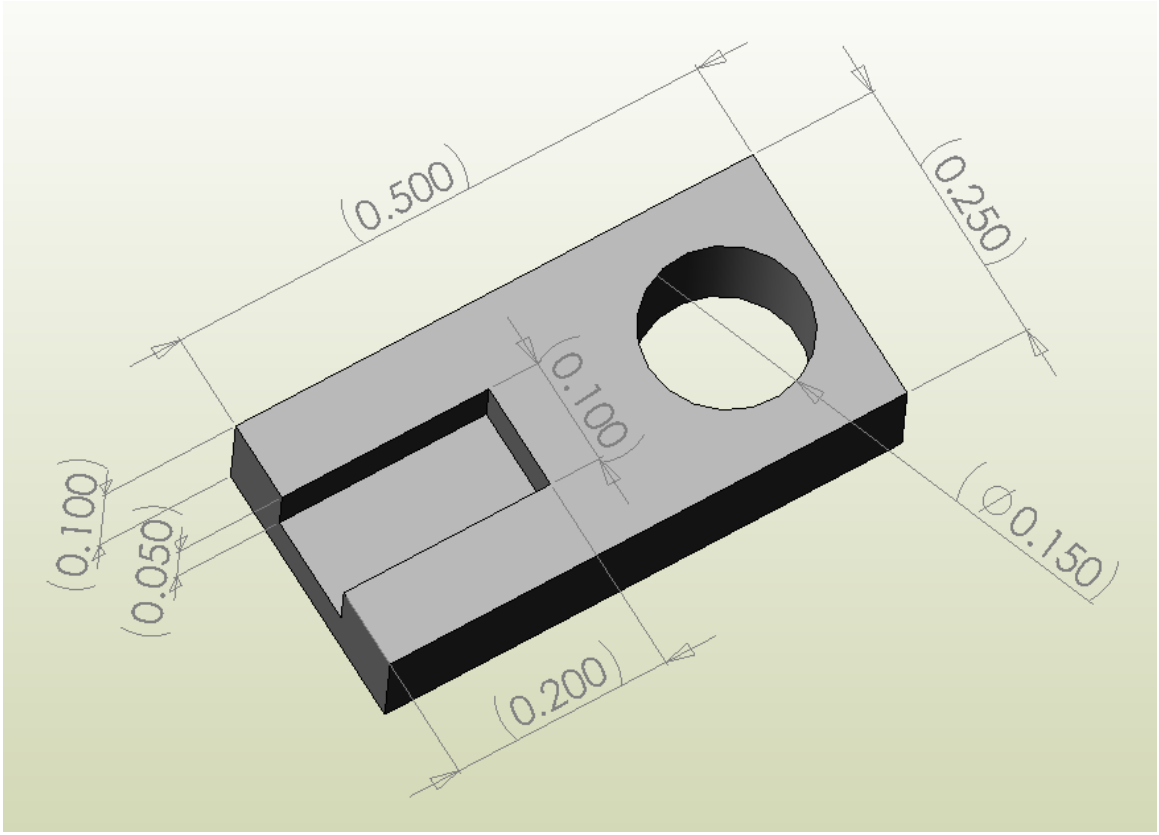

Figure 3.4 Cernox® Mount Design

Figure 3.5 OFHC Cernox® Mount

The pocket in the mounting fixture is lined with cigarette paper that is doped with GE varnish in order to provide electrical insulation. The adaptor plate and thermal plate are also covered with a layer of cigarette paper for insulation. The remaining volume between the chip and the pocket wall is filled with Apiezon® N cryogenic grease in order to ensure positive thermal contact.

The temperature sensor T3 is a CX-SD package that was previously mounted in a brass channel (for a different experiment) and secured with Stycast® epoxy. The brass mount is secured to the canister by means of a copper clip. A piece of Indium foil, coated with Apiezon® N, is sandwiched between the brass and copper in order to ensure adequate thermal contact. Figure 3.6 illustrates the sensor T3 mounted to the canister.

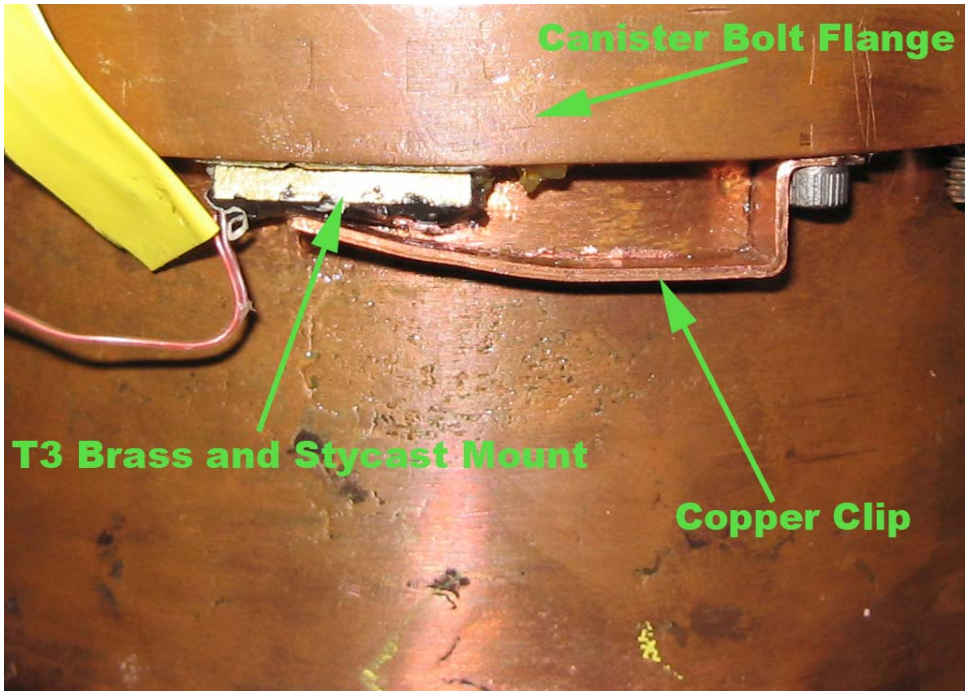

Figure 3.6 Cernox® T3 Canister Mount

3.1.2 Silicon Diode Mounting

The Silicon Diode is contained in a package type SD-CU copper bobbin mount shown in Figure 3.7.

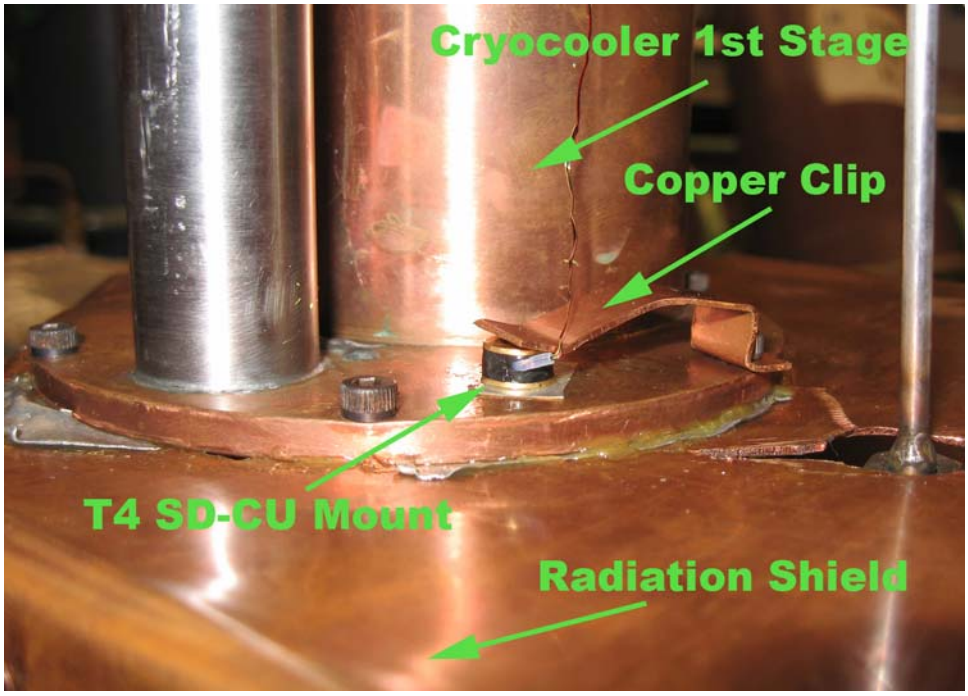

Figure 3.7 SD-CU Silicon Diode Mount

This mounting package can be attached using a single #4x40 screw; in this experiment, the sensor is attached using a copper clip in order to avoid drilling and tapping a hole into the first stage flange of the GB-04 cryocooler. Apiezon® N coated indium foil was again sandwiched between the sensor and the experiment.

3.1.3 Temperature Sensor Wiring

The four temperature sensors are wired to the data acquisition system using a four wire connection in order to eliminate measurement errors related to the lead resistance. A Hibelco hermetic feed through, shown in Figure 3.8, is used to make electrical connections into the vacuum space.

Figure 3.8 Hibelco Hermetic Feedthrough

The temperature sensor wiring diagram is summarized in Appendix B. A Lakeshore 218 Temperature Monitor is used to read the temperature sensor voltage (when energized with a known current). The 218 Temperature Monitor uses the manufacturer's sensor calibration information to convert the voltage to a temperature. The output temperature values are transferred with a National Instruments GPIB/A USB into a Labview user interface.

3.1.4 Electric Resistance Heater

The resistance heater serves two functions. First, it is used to maintain the temperature of the cryogen so that it will remain in a liquid state while filling occurs. The cryogen must be kept in a liquid state until the annulus is full because the thin fill lines into the annulus may otherwise become clogged with frozen cryogen. The heater is also used in conjunction with the thermometers to determine the power dissipated in the frozen cryogen through a calorimetric method. This calibration is accomplished in-situ using the heater. The heater is attached to the canister plate with a copper clip as shown in Figure 3.9.

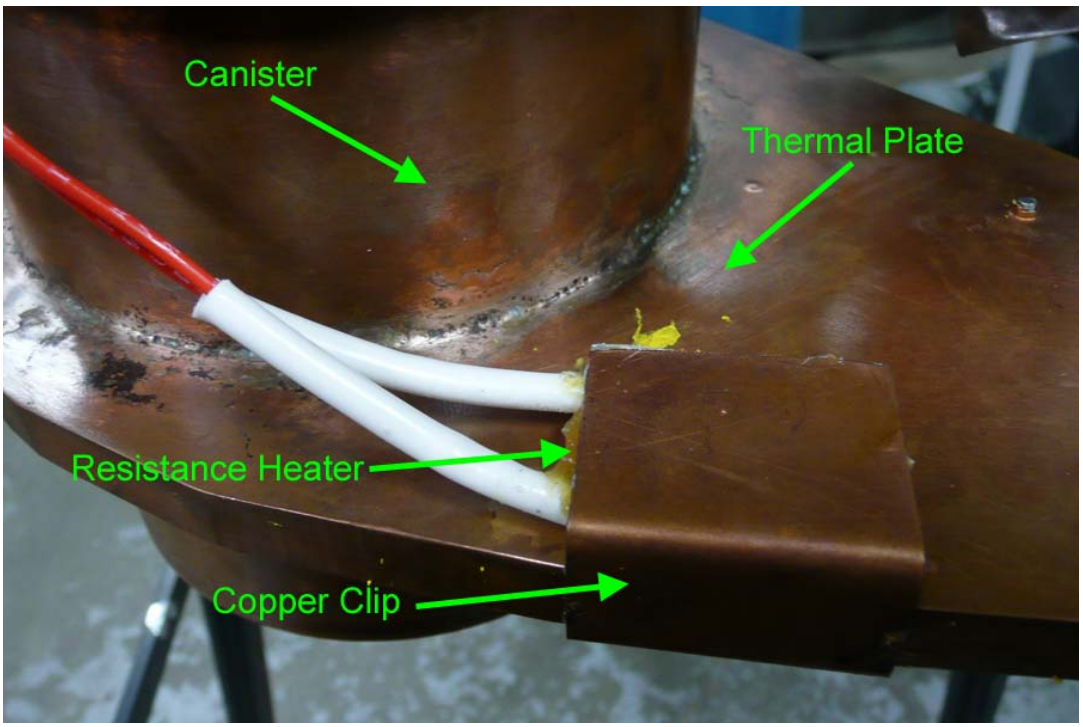

Figure 3.9 Electric Resistance Heater

The heater is mounted in a manner that is similar to the temperature sensors; a piece of indium foil is sandwiched between the heater and the canister plate in order to provide good thermal contact. The leads are passed outside the vacuum space through the hermetic feedthrough. The size of the heater is determined by the power that is required to maintain the cryogen in its liquid state. A target power of 20 W is estimated to be sufficient to overcome the cryocooler cooling power and raise the average annulus temperature above the cryogen's triple point based on the cryocooler load curve.

A commercial Hotwatt® heater is specified; the heater provides 50 W at 120 volts V. The current required at the rated power was calculated using the power formula:

$$P_{rated} = I_{rated}\ V_{rated} \tag{3.1}$$

where P_{rated} is the electric power of the heater and I_{rated} and V_{rated} are the rated current and voltage, respectively. Ohm's Law was then used to calculate the resistance (R) of the heater:

$$P_{rated} = I_{rated}^2\ R \tag{3.2}$$

Assuming that this resistance is nominally constant with power, the current required at the desired power of 20 watts ($P_{desired}$) is:

$$P_{desired} = I^2_{required}\ R \tag{3.3}$$

Table 3.1 summarizes the parameters and results of these calculations.

Table 3.1. Parameters and results of calculations for the electric resistance heater design

Parameter	Symbol	Value
Rated Power	P_{rated}	50 [W]
Rated Current	I_{rated}	0.417 [amps]
Rated Voltage	V_{rated}	120 [volts]
Heater Resistance	R	288 [ohms]
Desired Power	$P_{desired}$	20 [W]
Required Current	$I_{required}$	0.264 [amps]
Required Voltage	$V_{required}$	75.76 [volts]

A Harrison 60 volt variable power supply is employed to supply the current. The power supply maximum voltage is just under the estimated voltage required, but it was deemed close enough for use. If the power required is greater than the power supply can provide, a new power supply can replace the unit.

3.1.5 Calorimetric Calibration

An in-situ calorimetric calibration is performed in order to determine the relationship between energy dissipated in the annulus and the change in average annulus temperature. The exact annulus temperature is uncertain due to the uncertainty in the temperature profile across the annulus. Therefore, the annulus and thermal plate were modeled in ANSYS®, a commercial finite element analysis (FEA) program [7]. The resulting temperature profile is shown in Figure 3.10.

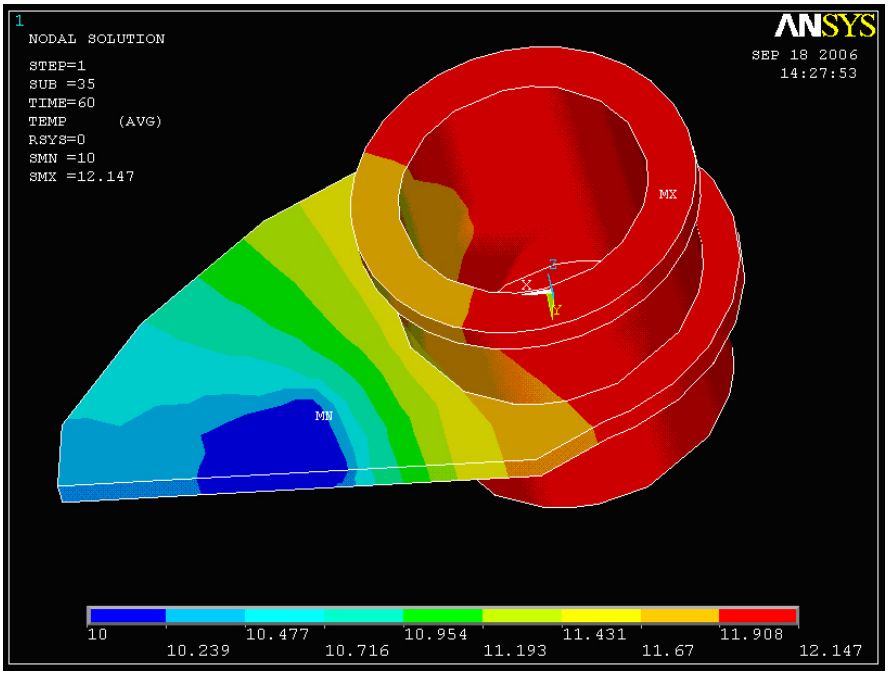

Figure 3.10 ANSYS® FEA Annulus Temperature Profile

The ANSYS® model is used to estimate the coldest annulus temperature, which is used in the calibration. The coldest temperature is calculated by subtracting the temperature difference across the ANSYS® profile (~1.0 [K]), from the location of the temperature sensor at the upper back side of the canister (T3), to the coldest location on the annulus (the junction of the canister and thermal plate closest to the cryocooler).

The calibration must be performed for each test cryogen because the different cryogens will affect the annulus temperature change due to power input. The change in average annulus temperature is calculated and plotted against the heater input power as shown for the deuterium and neon calibration in Figures 3.11 and 3.12 respectfully.

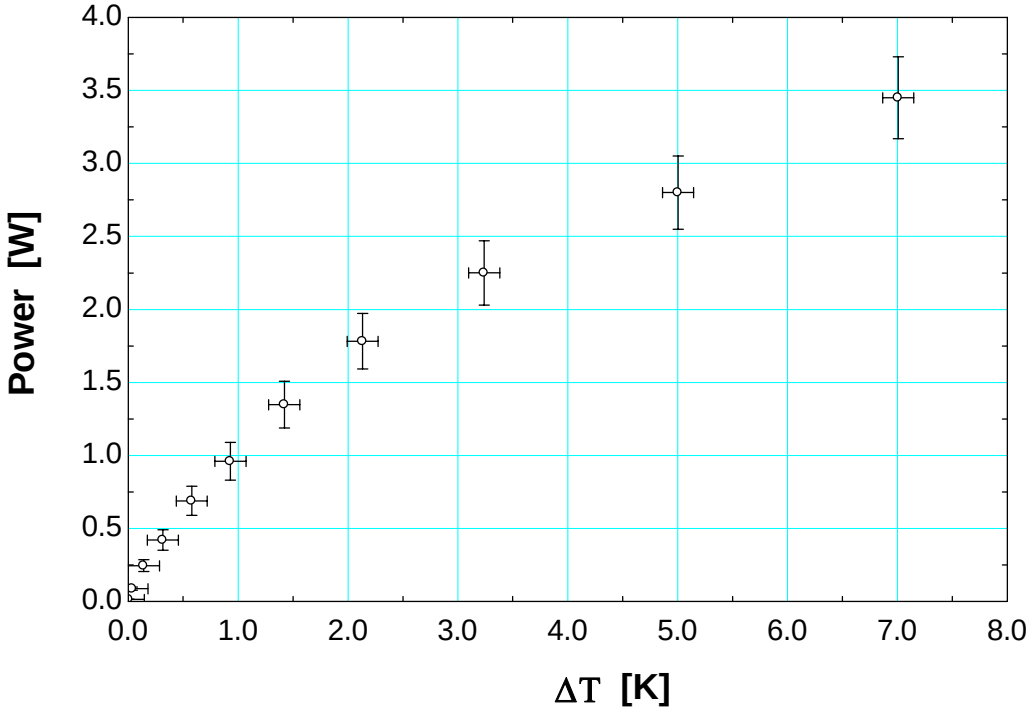

Figure 3.11 Deuterium Calorimetric Calibration Curve

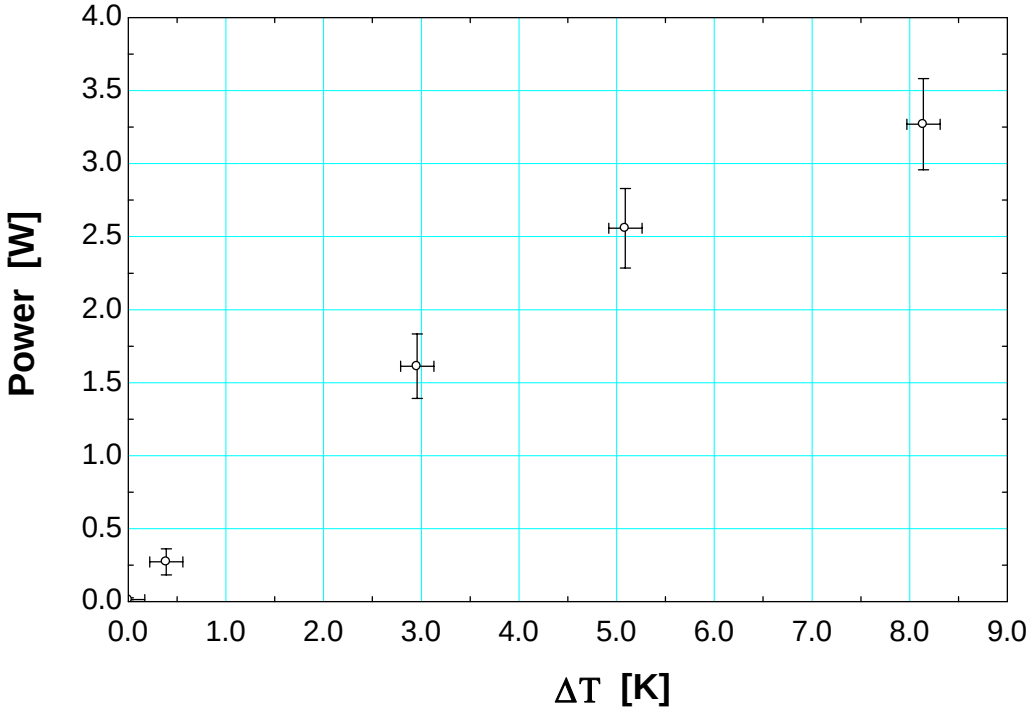

Figure 3.12 Neon Calorimetric Calibration Curve

The resulting calibrations are non-linear due to the change in conductivity of the stainless steel drive shaft, which is the main path for heat leak.

The calibration is subject to uncertainties in measurement of the input power and the temperature change in the annulus. The input power uncertainty is a combination of the measured voltage and measured current, which are estimated to be 0.01 [volts] and 0.01 [amps] respectively. The temperature change uncertainty is a combination of two Cernox temperature measurements that have an estimated uncertainty of 0.1 [K] and the ANSYS® model that has an estimated uncertainty of 0.1 [K]. Formulas used in the uncertainty analysis for the calorimetric calibration are found in Appendix C.

3.2 Mechanical Measurement System

The mechanical measurement system is comprised of a load cell and rotational speed encoder. The load cell is used to measure the reaction torque on the motor due to the shear force on the shaft. The rotational speed encoder is used to measure the rotation rate of the cylinder. The shaft power ($\dot{W}_{shaft}$) is related to the motor torque (T_{shaft}) and angular velocity (N, in rev/s) according to:

$$\dot{W}_{shaft} = 2\pi \; N \; T_{shaft} \tag{3.4}$$

3.2.1 Motor Pivot

A horizontal turntable with a hole through its axis of rotation serves as a support carriage for the motor housing and allows the motor's shaft to penetrate through its central hole. The configuration enables the torque, required by the motor's shaft to turn the solid

copper cylinder within the canister, to be measured through its reaction against the turntable. A set of bearing packs between the dewar structure and the turntable permits the turntable to rotate smoothly. The motor carriage is shown in Figure 3.13.

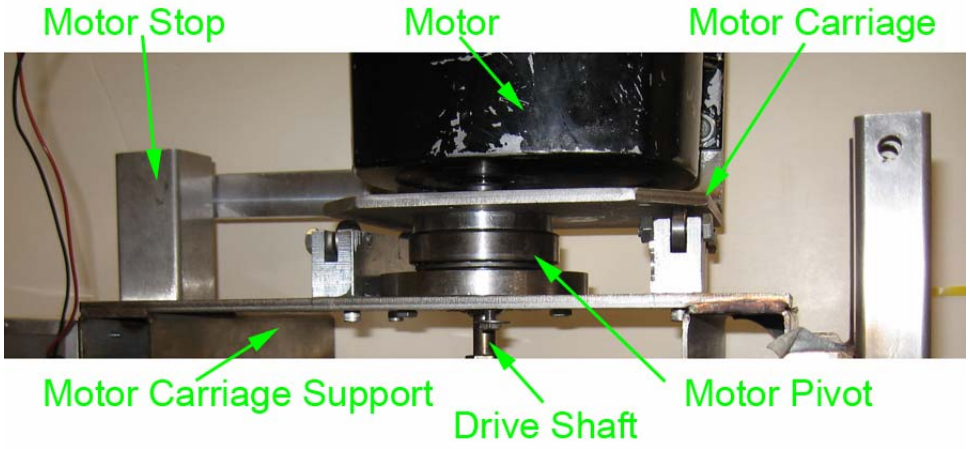

Figure 3.13 Motor Carriage

The bottom of the bearing is mounted on a 6.35 mm (0.25 in.) stainless steel plate welded to support legs that are bolted to the stainless adapter flange. It is critical that the legs not twist under load, so they are made from 50.8 mm (2 in.) square stainless steel tubing. Additional small bearings are used to support the edge of the motor carriage so that it rests stably on the turntable. The motor support carriage is shown in Figure 3.14.

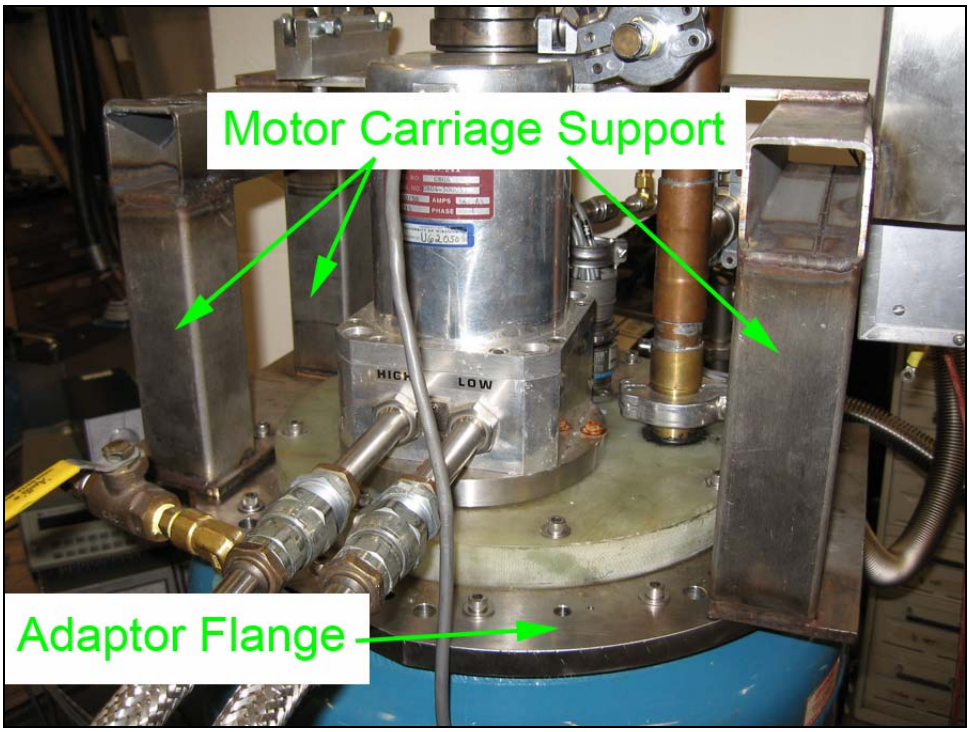

Figure 3.14 Motor Carriage Support

3.2.2 Strain Gage Load Cell

A load cell used to measure beam deflection is fabricated using two strain gages that are installed on a 6061 aluminum bar. The bar is mounted to the same turntable that supports the motor, and prevents the turntable / carriage from turning freely because its other end encounters a mechanical stop that is welded to the motor carriage support structure. Instead, the mechanical stop causes the bar to deflect and the resulting bar deflection (strain) is related to the applied torque. The system is shown in Figure 3.15.

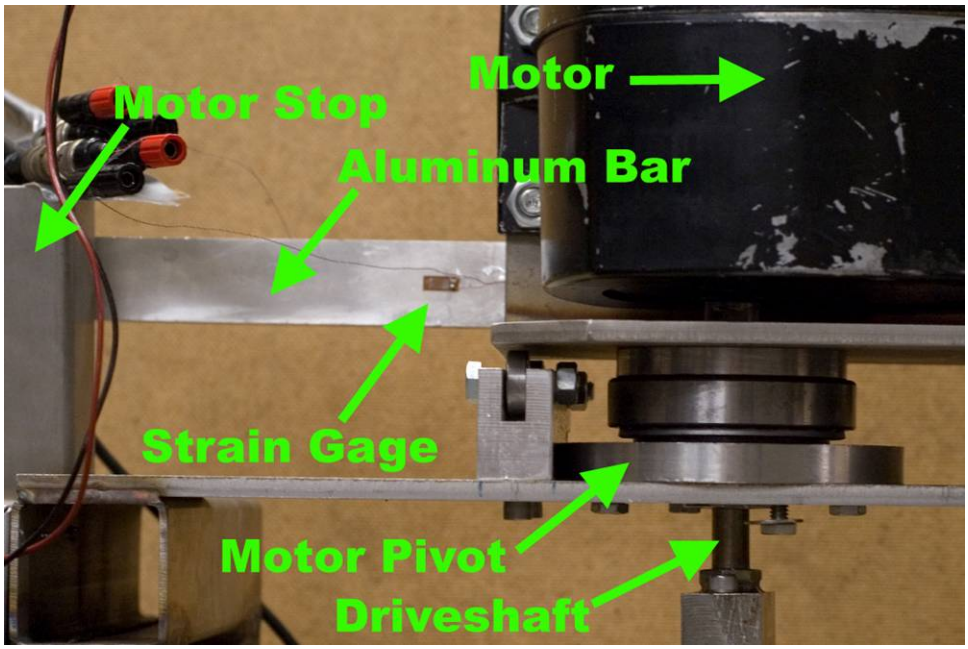

Figure 3.15 Strain Gage Load Cell

The geometry used for the bar was selected in order to provide a reasonable signal (i.e., a measurable output voltage from the strain gages interfaced with a Wheatstone bridge) while still maintaining the stress below the yield strength of aluminum. A set of stress calculations have been performed in order to determine appropriate dimensions for the aluminum bar, and the associated strain that will be induced on the strain gages.

The stress (σ_{Al}) in a beam subjected to a bending moment at one end is calculated by a basic mechanics of materials bending beam analysis [13]:

$$\sigma_{Al} = \frac{M_{Al}\ y_{Al}}{I_{Al}} \tag{3.5}$$

where M_{Al} is the bending moment applied to the bar, which is related to the force applied to the bar (F_{Al}) and the distance, with respect to the axis of rotation, where the force is applied (d_{Al}),

$$M_{Al} = F_{Al}\, d_{Al} \tag{3.6}$$

y_{Al} is the distance from the shear axis, which in this load case is the center of the bar, to the location of interest (the outer edge, where the stress is largest), which is a function of height of the aluminum bar (h_{Al}) in the direction of bending ,

$$y_{Al} = \frac{h_{Al}}{2} \tag{3.7}$$

and I_{Al} is the moment of inertia for a rectangular cross section, which is a function of aluminum bar base thickness (b_{Al}), and height:

$$I_{Al} = \frac{1}{12} b_{Al}\ h_{Al}^3 \tag{3.8}$$

The normal stress induced in the beam is related to the strain (ε_{Al}) by the modulus of elasticity, E_{Al} = 70 GPa [13] for aluminum:

$$\sigma_{Al} = E_{Al}\ \varepsilon_{Al} \tag{3.9}$$

The strain on the bar is measured by a pair of strain gages with a nominal resistance of 350 ohms that are affixed to the aluminum bar with cyanoacrylate glue, as shown in Figure 3.16.

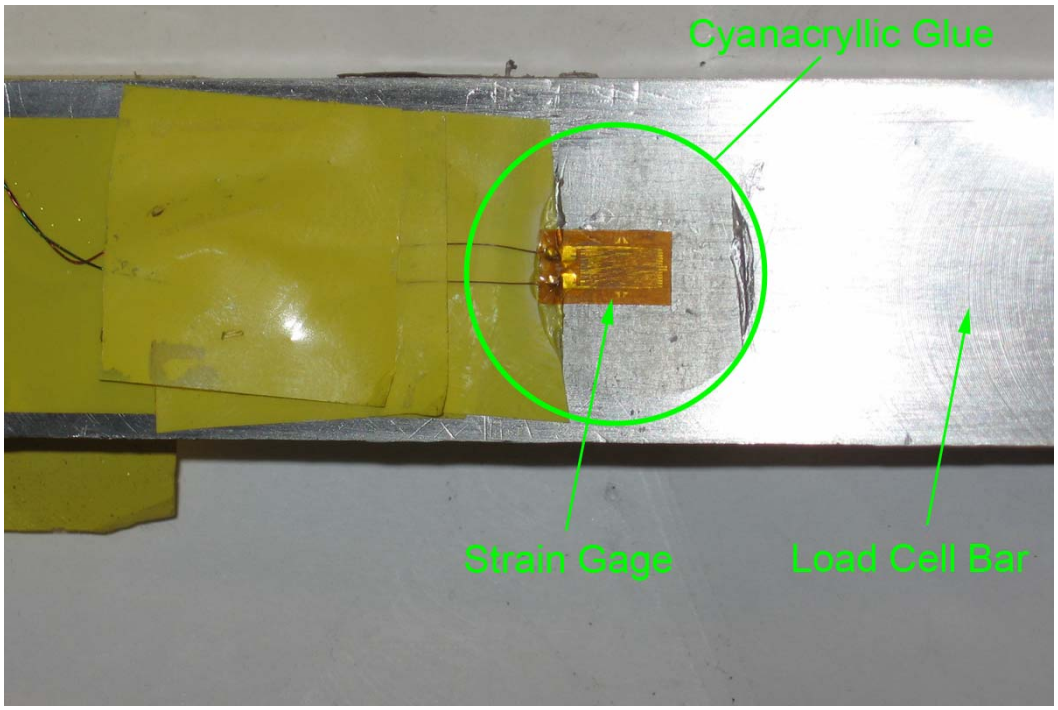

Figure 3.16 Strain Gage Mounting

The gages are placed on either side of the beam and oriented so that one gage sees a pure tensile strain while the other sees a pure compressive strain. The tensile strain causes an increase in the gage resistance while the compressive strain causes a reduction in the gage resistance. The strain gages are connected to a Wheatstone bridge so that the strain on both gages will combine to give maximum output voltage. This is accomplished by attaching the strain gages in the configuration of the bridge shown in Figure 3.17.

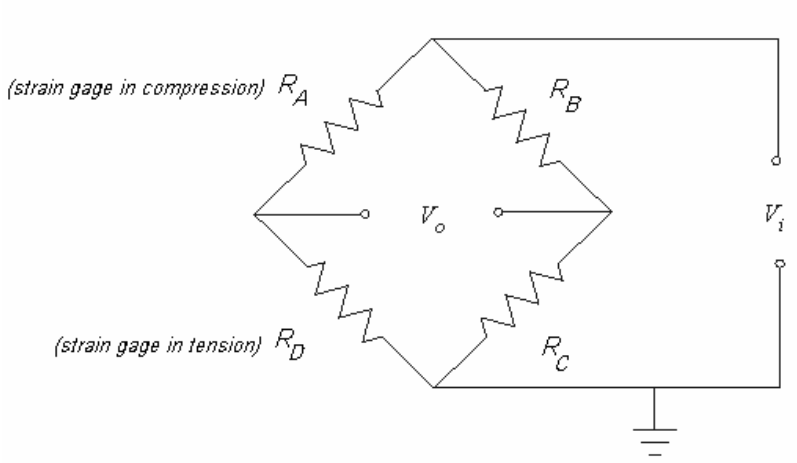

Figure 3.17 Wheatstone Bridge Configuration

The output voltage can be predicted by performing a circuit analysis on the bridge. Both sides of the bridge act as a voltage divider. Therefore, the ratio of the output voltage to the input, or excitation voltage, can be related to the resistances of the strain gages according to:

$$\frac{V_o}{V_i} = \frac{R_D + \Delta R_D}{R_A + \Delta R_A + R_D + \Delta R_D} - \frac{R_C}{R_B + R_C} \tag{3.10}$$

where R_A and R_D are the nominal resistances of the strain gages in compression and tension (respectively) while ΔR_A and ΔR_D are the strain induced changes in these resistances. As the bar is deflected, the change in strain gage resistance leads to a change in the measured output voltage. Note that when there is no deflection, (i.e., ΔR for both strain gages are zero) the ratio of the internal bridge resistors is adjusted to produce a zero output voltage. Thus the Wheatstone bridge can be referred to as a "null" instrument, which characteristic allows for a very accurate observation of very small changes in

resistance. Shielded, twisted pair wires connect a National Instruments USB-6009 data acquisition system to the strain gages. LabView, through the USB-6009 system, provides the 10 volt DC excitation voltage to the Wheatstone bridge, and also records the DC output voltage from the Wheatstone bridge.

The change in strain gage resistance (ΔR) is related to the strain by:

$$\Delta R = R_{nom}\ GF\ \varepsilon_{Al} \tag{3.11}$$

where(R_{nom}) is the strain gage nominal resistance, and (GF) is the gage factor.

The bar dimensions include the length (d_{Al}) and height (h_{Al}). The length is constrained by the distance from the motor carriage to the motor stop and the thickness is selected based on availability so that it is consistent with an existing aluminum bar with the required length. The base thickness of the aluminum bar (h_{Al}) free parameter is varied to determine the stress in the bar, which results in a strain, and thus change in resistance in the strain gages that is large enough to measure.

The height of the bar is selected so that the maximum output voltage of 0.025V is achieved without exceeding the yield stress of the aluminum bar (165 MPa [13]). The bar height optimization is shown in Figure 3.18.

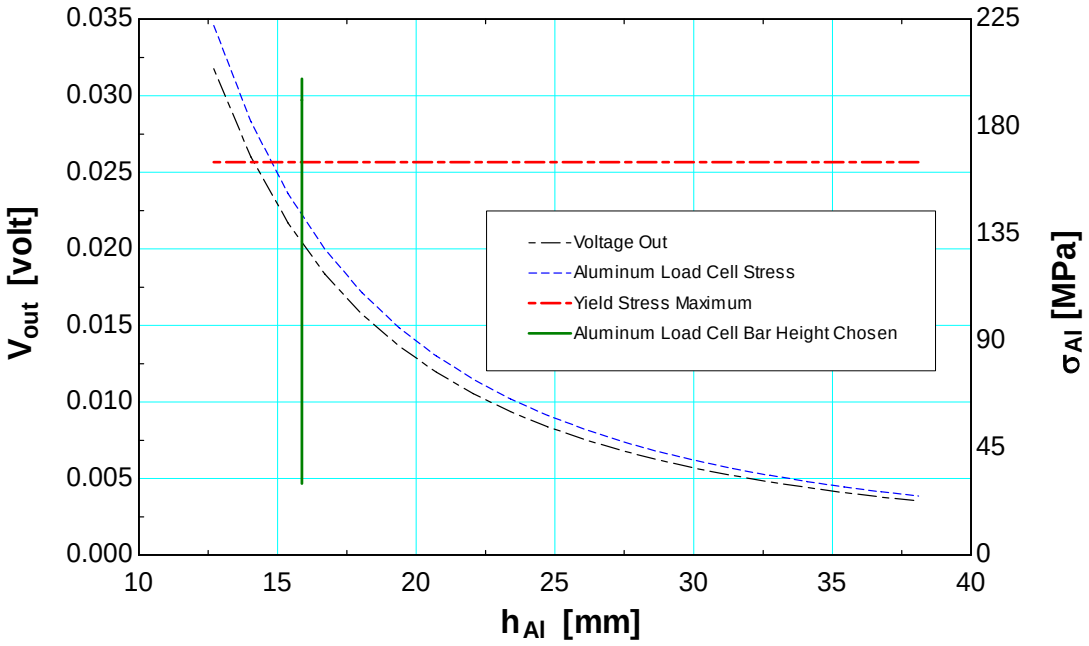

Figure 3.18 Load Cell Bar Height Optimization

The final dimensions for the bar are 31.75 mm x 15.88 mm x 304.8 mm (1.25 in. x 0.625 in. x 12 in.). The stress formula parameters and calculation results are summarized in Table 3.2.

Table 3.2. Parameters and results of calculations for the stress formula

Parameter	Symbol	Value
Load Cell Bending Stress	σ_{Al}	35.58 [Mpa]
Load Cell Bending Moment	M_{Al}	94.91 [N-m]
Distance from the Shear Axis to the Normal Stress	y_{Al}	15.875 [mm]
Applied Force	F_{Al}	311.4 [N]
Distance of the Applied Force (Length of Load Cell)	d_{Al}	30.48 [mm]
Load Cell Height	h_{Al}	31.75 [mm]
Load Cell Moment of Inertia	I_{Al}	4.23E-8 [m4]
Load Cell Base Thickness	b_{Al}	15.88 [mm]
Aluminum Modulus of Elasticity	E_{Al}	70 [Gpa]
Load Cell Strain	ε_{Al}	5.08E-4 [mm/mm]
Change in Strain Gage Resistance	ΔR	0.3558 [ohm]
Nominal Strain Gage Resistance	R_{nom}	350 [ohm]
Gage Factor	GF	2

Equations (3.5) through (3.11) were used to design the torque measurement system. However, these equations are not subsequently used to interpret the output voltage and relate it to the applied torque. Rather, the torque measurement system is calibrated in-situ in order to eliminate uncertainties in dimensions, strain gage characteristics, and material properties. To conduct the in-situ calibration, the motor stand must first be secured to the test bench with C-clamps. The motor is set on the motor pivot, and the calibration bar is coupled to the motor. A cable is secured to a point six inches from the calibration bar pivot point and fed across a pulley, down towards the ground and fastened at the other end to a 'weight bucket' as shown in Figure 3.19.

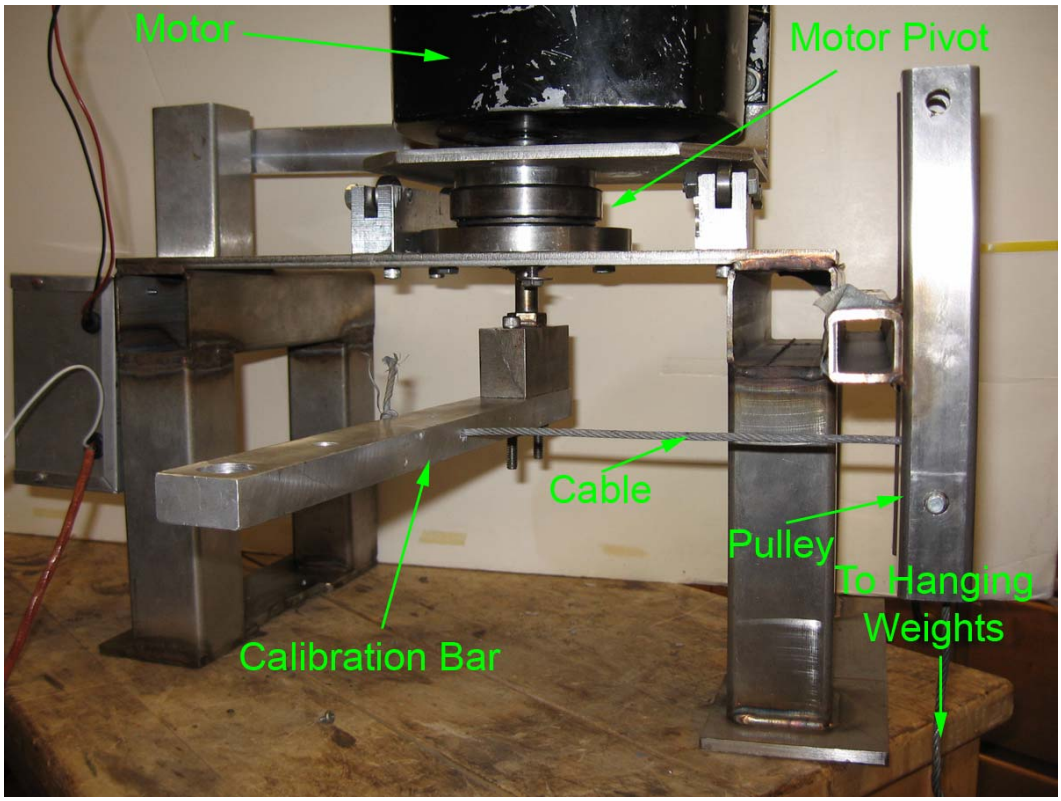

Figure 3.19 Load Cell Calibration Bar Setup

The strain gages are connected to the Wheatstone bridge and Labview is started. The load cell is calibrated by sequentially adding weights of known mass to the bucket and recording the output voltage from the Wheatstone bridge at each step. An example set of measurements from one such calibration is shown in Figure 3.20.

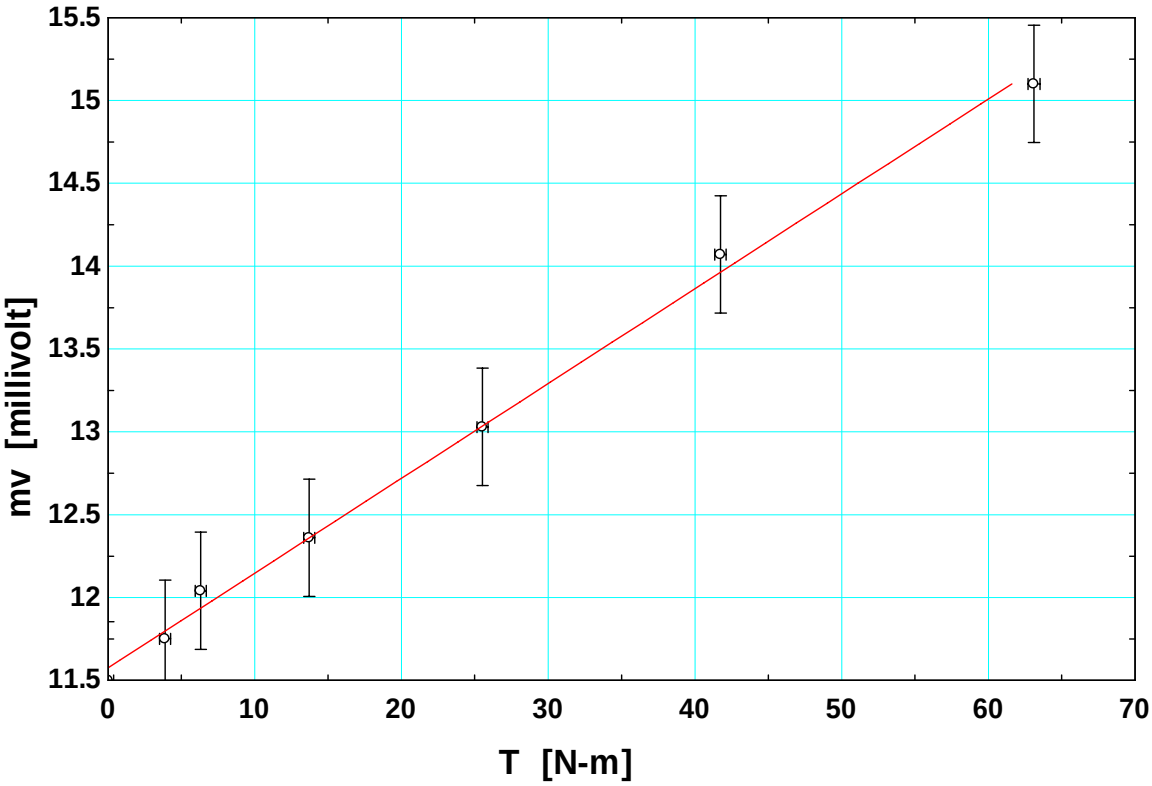

Figure 3.20 Load Cell Calibration

The calibration is subject to errors in measurement of the torque applied to the bar and the Wheatstone bridge voltage. The torque error is a combination of the applied load error and the error in the distance the load is applied, which are estimated to be 1 [N] and 0.001 [m] respectively. The Wheatstone bridge voltage is an average of upper and lower

voltage readings due to cyclic variation in the signal (see Chapter 5). Both the upper and lower voltage readings have an estimated error of 10 [mV]. Detailed uncertainty analysis for the load cell calibration is found in Appendix D.

3.2.3 Angular Velocity Measurement

The angular velocity is measured using a Honeywell 0502c magnetic switch, shown in Figure 3.21.

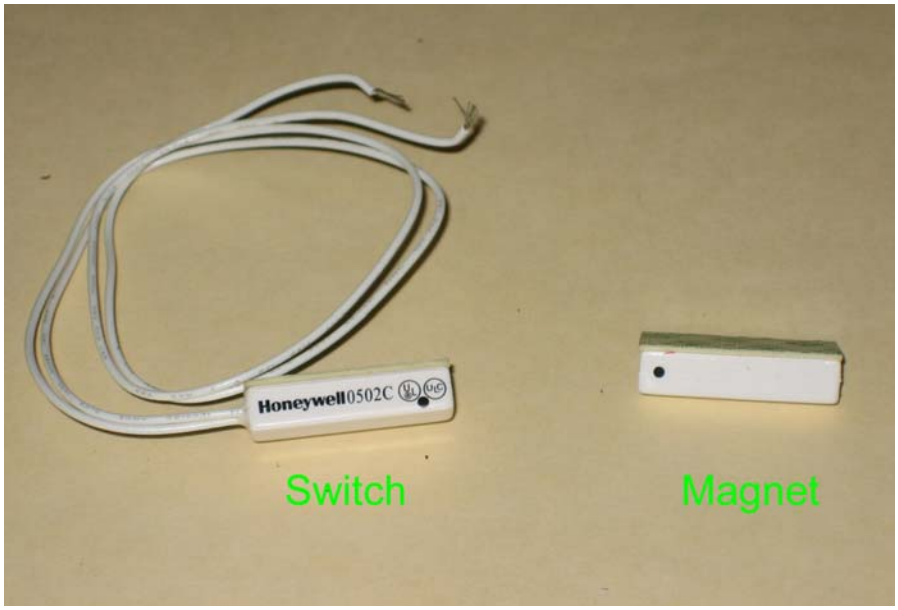

Figure 3.21 Honeywell 0502c Magnetic Switch

The switch is designed to close when it is exposed to a magnetic field and therefore complete a circuit. The switch is attached to the motor support and the magnet is glued to the drive shaft. The rotation of the drive shaft causes the magnet to periodically come into close proximity with the switch. The switch closes and remains closed until the magnet has rotated past the switch. The magnetic switch circuit is completed in a National Instruments data acquisition system and state of the switch is recorded by

LabView (the circuit voltage is recorded as a function of time). The circuit is shown in Figure 3.22.

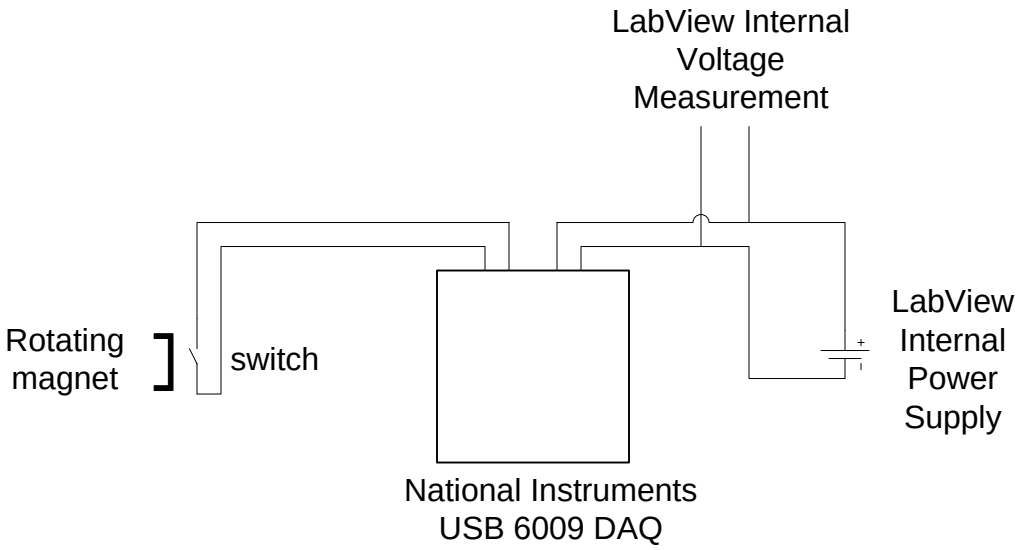

Figure 3.22 Rotary Encoder Circuit

The resulting square waveform is shown in Figure 3.23.

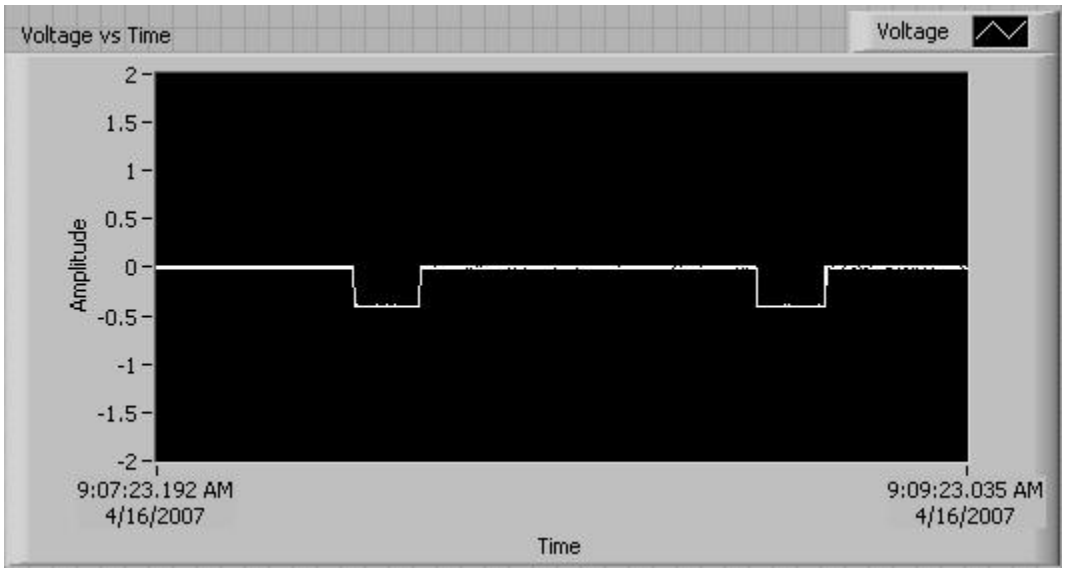

Figure 3.23 Square Waveform Measured using LabView

The time to complete one revolution is calculated by measuring the time between the leading edge of sequential waves.

The uncertainty in the rotation rate measurement is the error in measuring the time it takes to complete one revolution, which is estimated to be 0.5[s] (0.008 [min]).

Chapter 4 Experimental Operation

Measurements are gathered with each of the cryogens using the following procedure.

4.1 Torque Calibration

As previously described, the combination of torque and rotation rate measurements provide one of the two methods for determining the power dissipated by the frozen cryogen in the annular gap. The torque calibration is performed prior to final assembly of the motor upon its stand. The voltage developed at the Wheatstone bridge is recorded for each weight and plotted against the associated torque.

.

4.2 Annulus Purging

It is critical that all residual air be removed from the annulus in order to prevent the small diameter fill lines from becoming blocked with frozen air or moisture during the cool down process. To adequately purge the air from the annulus, it is evacuated and refilled with the desired pure gas several times while the entire system is at room temperature. Initially, the entire fill plumbing is evacuated to 10^{-3} [torr]. The fill valve is closed and

the evacuation valve is opened. The annulus is again evacuated to 10^{-3} [torr]. The annulus is then pressurized with the cryogen gas to 2.5 [psig]. This process is repeated six times to ensure all residual air is purged from the system. The final charge pressure is maintained at 2.5 [psig].

4.3 Cool Down Procedure

The procedure for filling the annulus with a solidified cryogen begins with the region charged with the associated gas, and all valves between the annulus and supply cylinder open. The cryocooler is turned on. As the gas in the annulus cools, its density increases, resulting in a flow of gas from the supply cylinder to the annulus. The flow of gas is monitored on the rotameter to ensure there is no blockage in the fill lines. The temperature of the annulus is allowed to drop to the saturation (or boiling) point of the gas, at which time the gas condenses to liquid and a constant temperature is observed. While the gas is condensing, the flow rate measured by the rotameter is at its largest value. When the annulus is filled with liquid the annulus temperature again decreases to the triple point, at which time the liquid solidifies and again the temperature remains constant during the phase transformation. After all the liquid is solidified, the temperature once more decreases, to the coldest possible system temperature, which is determined by the balance between the heat leak to the cryocooler and its cooling capacity.

4.4 In-Situ Calorimetric Calibration

The second method for measuring the dissipated power is accomplished via the temperature measurements on, and nearby, the annulus. The calorimetric method is enabled by an in-situ calibration of the thermometer signals, and is conducted separately for each cryogen. In the first step of the calibration procedure, a known amount of power is applied to the heater mounted on the copper plate that connects the annulus to the cryocooler. The power is slowly increased until a steady state annulus temperature is reached that is in the range above the triple point and below the boiling point. It is important to raise the power in small steps because, due to the spatial distance between the heater and thermometers, and the large thermal mass of the copper plate and annulus, it is possible for the annulus temperatures to continue increasing above the boiling point even after the power supplied to the heater is shut off. In such a situation, the liquid boils, the pressure in the annulus rises above the set point of the pressure relief valve, and the gas is vented to the room. The expense associated with deuterium gas makes this a very undesirable event. In the case where venting is avoided, the power to the heater is reduced in discrete steps until it is completely removed. For each value of heater power, steady state conditions are established before recording the calibration point. The power to the heater input is plotted against the thermometer signals to create the calibration curve.

4.5 Test Steps

The energy dissipation measurements begin by adjusting the heater power in order to bring the temperature of the annulus above the cryogen's triple point, but below its

boiling point. Once the cryogen is in the liquid state, it is allowed to "soak" for 30 minutes to ensure that the entire annulus is liquid. The motor is then turned on and the speed controller is adjusted to a pre-determined motor rotation rate. The heater power supply is subsequently reduced in discrete steps in a similar manner to that used in the calorimetric calibration. The temperatures and strain gage voltages are recorded for each step in order to compare them to the calorimetric and torque calibrations. The process is repeated for multiple rotation rates.

Chapter 5 Experimental Results and Discussion

5.1 Preliminary Tests

Imperfections in the drive shaft and inner cylinder concentricity, combined with temperature gradients across the annulus, resulted in a time varying Wheatstone bridge signal as shown in Figure 5.1.

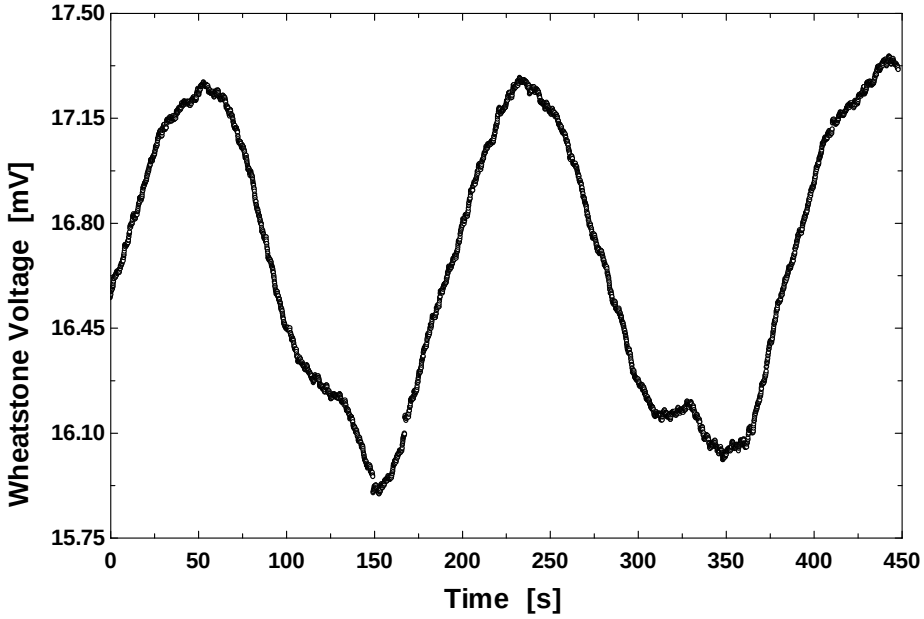

Figure 5.1 Wheatstone Bridge Signal from 0.74 RPM Neon Test

The average of the voltage signal was used to determine the associated value of torque.

Preliminary tests were performed with deuterium to provide a rough estimate of how the cryogen would react under different test schemes. These revealed that if the motor was turned on while the deuterium was still liquid and the deuterium was then allowed to cool, a slight torque increase was observed. However, if the deuterium was first allowed to freeze and cool to below its triple point with no rotation, and then the motor was turned on, very large torque (> 160 N-m) values, even exceeding the yield strength of the drive shaft, could develop.

5.2 Multiple Cryogen Energy Dissipation Results

A second set of tests were carried out first with neon, and then again with deuterium. In these, initial steady state conditions are established with the cryogen in the liquid state

and with the inner cylinder turning at a constant non-zero rotation rate. Continual measurements of temperature and torque are gathered while the heater power is decreased in a step-wise manner, allowing equilibrium conditions to be established over a 1/2 hour period at each value of heater power.

In the measurements gathered with non-zero rotation, the average annulus temperature is observed to remain in the liquid range, even when the heater power is reduced to zero. Figure 5.2 displays schematically the interpretation of this data. Here the temperatures displayed correspond to the neon tests.

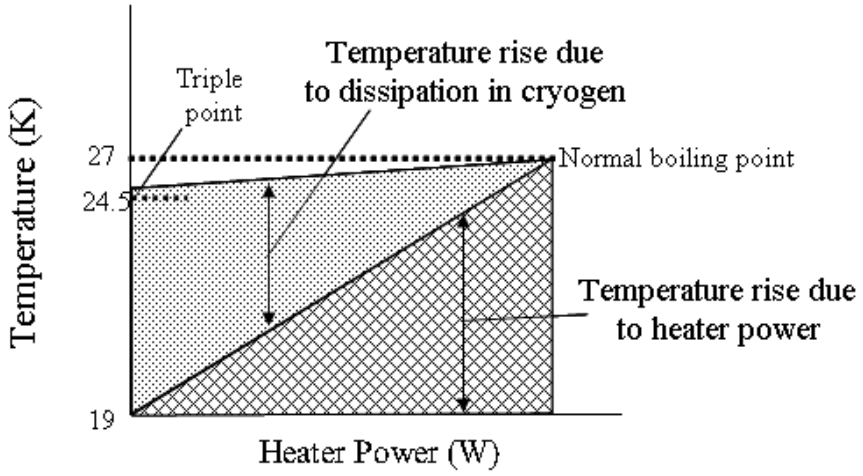

Figure 5.2 Heater Power Subtraction and Resulting Dissipation

That is, as the delivered heater power is reduced, the dissipation increases so that the sum of the delivered and generated power maintains the average temperature of the neon in its liquid regime. Subtracting the applied heater power at each step from the total power, yields the power dissipated by viscous or sheer forces. The total power is determined from the prior in-situ calorimetric calibration (see Figures 3.11 and 3.12).

Power dissipation with non-zero rotation is also calculated by measuring the rotation speed and reaction torque at the motor. The prior in-situ calibration of the strain gauges is used to determine the reaction torque of the motor (see Figure 3.20). The average strain gage signal recorded during experimental operation is converted to a total torque, which combined with the measured rotation rate provides the total power. An offset power, dissipated by the system when the annulus is empty, is subtracted from the total system power to yield the power from the dissipation in the cryogen alone.

The energy dissipation results at 0.74 rpm for neon and deuterium are shown in Figure 5.3. Additional hydrogen comparison data points, determined from previous work by Andraschko [7], are also included.

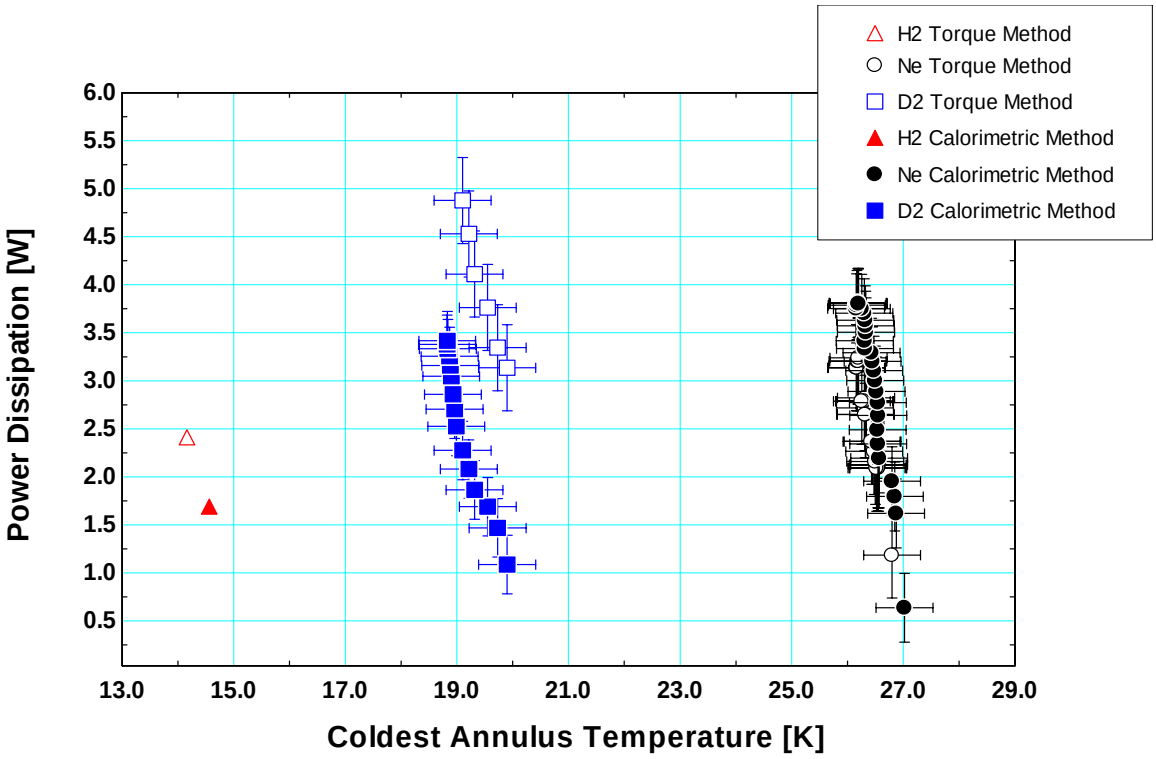

Figure 5.3 Energy Dissipation Results for Neon, Deuterium, and Hydrogen

5.3 Energy Dissipation Results for Multiple Rotation Rates

Extensive tests were completed with deuterium for multiple rotation rates ranging from 0.27 rpm to 2.50 rpm. The results of the energy dissipation calculation by the torque and calorimetric methods are shown in Figures 5.4 and 5.5 respectfully.

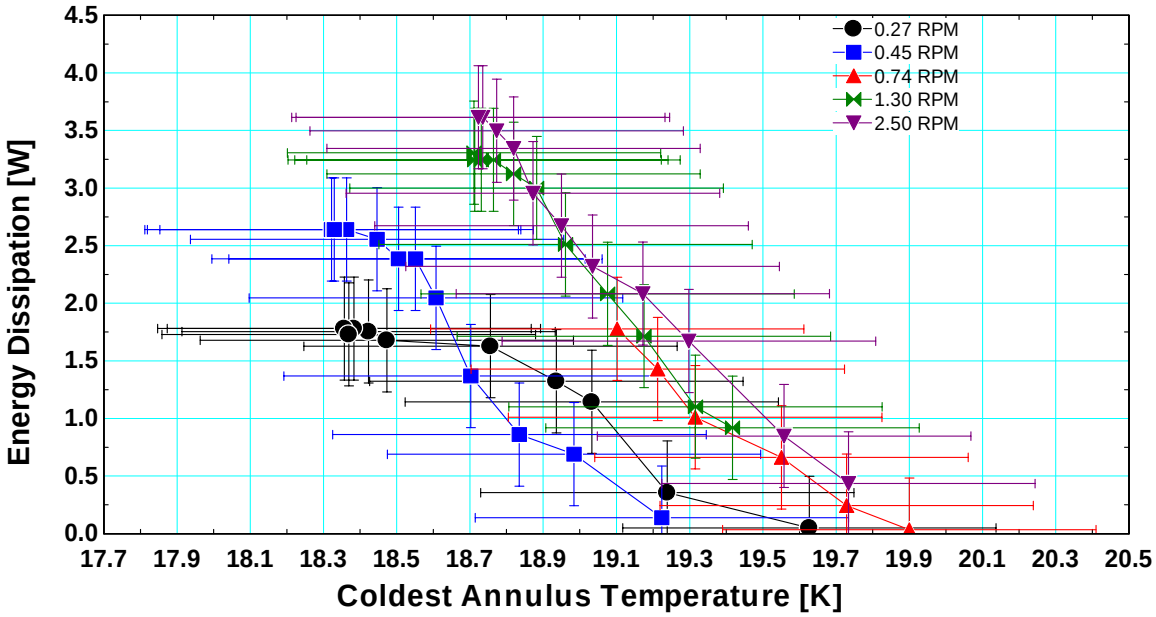

Figure 5.4 Torque Method Energy Dissipation Results for Multiple Rotation Rates with Deuterium

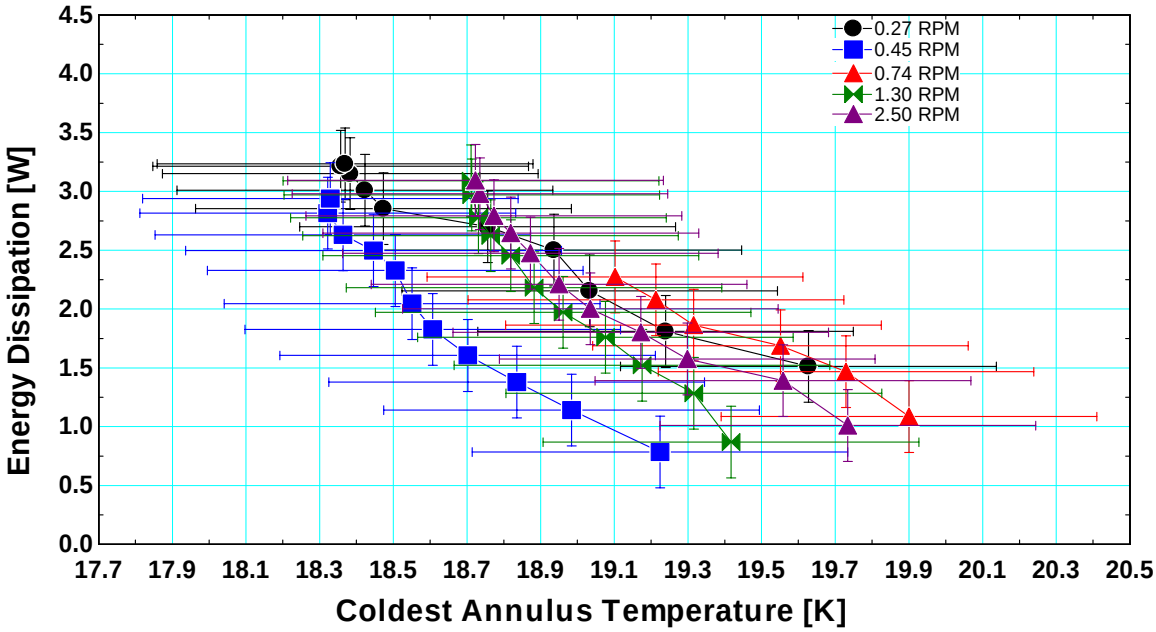

Figure 5.5 Calorimetric Method Energy Dissipation Results for Multiple Rotation Rates with Deuterium

The energy dissipation calculated by the torque method is subject to uncertainties in the load cell calibration and rotation rate. The dissipation results are plotted against the coldest annulus temperature, which uncertainty contributions from the measurement of T3, and the temperature profile predicted by the ANSYS® model. The vendor calibration of T3 has an absolute uncertainty of $\pm$ 0.1 [K], while that associated with the temperature profile determined from an ANSYS® model is estimated at $\pm$ 0.5 [K].

The energy dissipation calculated by the calorimetric method is subject to errors in the calorimetric calibration, and the measurement of the annulus temperature change caused by the dissipation. Like the torque method, the results are plotted against the coldest annulus temperature which has the same uncertainty as stated previously. Detailed uncertainty analysis for the energy dissipation calculation is found in Appendix E.

5.4 Viscosity Results

Based on the energy dissipation data in Figure 5.3 derived with the torque method and from the equation for energy dissipation due to viscous forces,

$$q_{visc} = \mu\left(\frac{\pi D n}{h}\right)^2 V \tag{5.1}$$

the viscosity of (presumably) slush neon ranges from $1.1\text{x}10^4$ to $8.8\text{x}10^4$ kg/m-s. In equation (5.1), μ is the dynamic viscosity, D is the cylinder diameter, n is the rotation rate, h is the annular gap distance, and V is the annular volume. These values are 8 orders of magnitude larger than those for liquid neon.

In a similar manner, data from Figure 5.4 is used to calculate the viscosity of (presumably) slush deuterium shown in Figure 5.6.

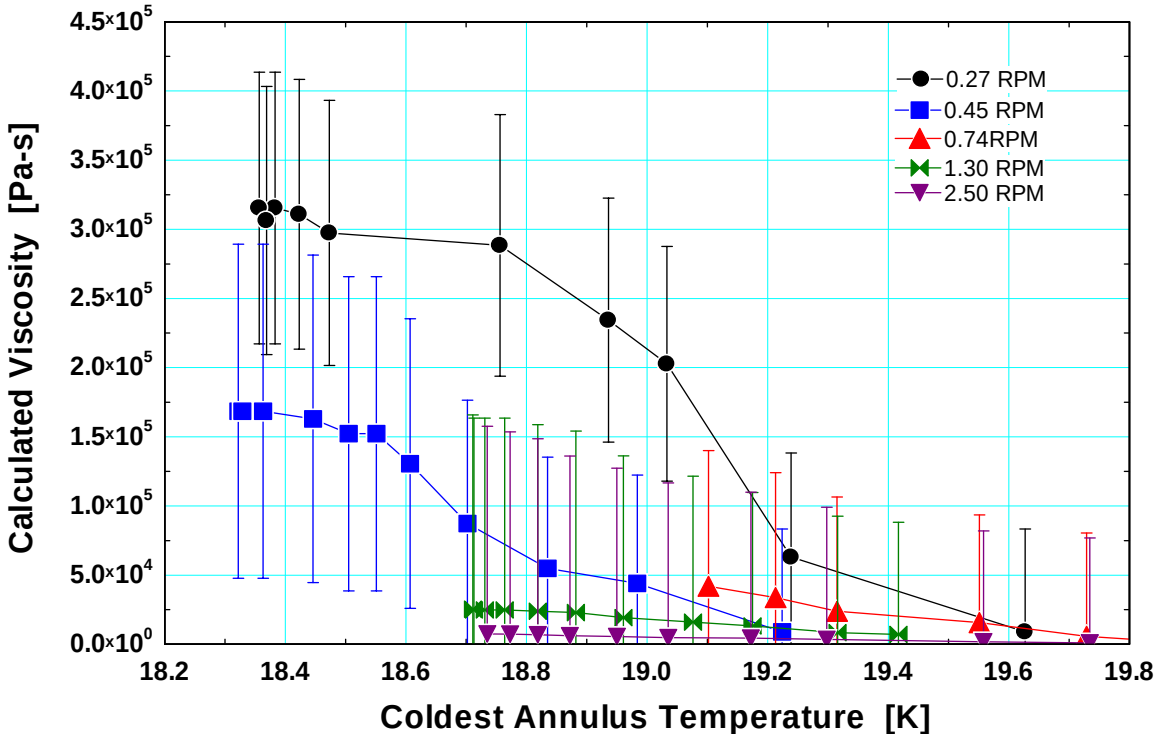

Figure 5.6 Viscosity Results for Multiple Rotation Rates with Deuterium

The viscosity values are subject to uncertainties in the estimated energy dissipation, cylinder diameter, rotation rate, gap height, and annulus volume. The energy dissipation and rotation rate are the previously mentioned values (see Sections 5.3 and 3.2.3 respectively). The cylinder diameter and gap height each have an estimated uncertainty of 0.0005[m], and the annulus volume has an estimated uncertainty of 0.0009[m^3]. Detailed uncertainty analysis for the viscosity calculation is found in Appendix F.

The results, compared to viscosity values estimated by Viniar [8], are shown in Figure 5.7.

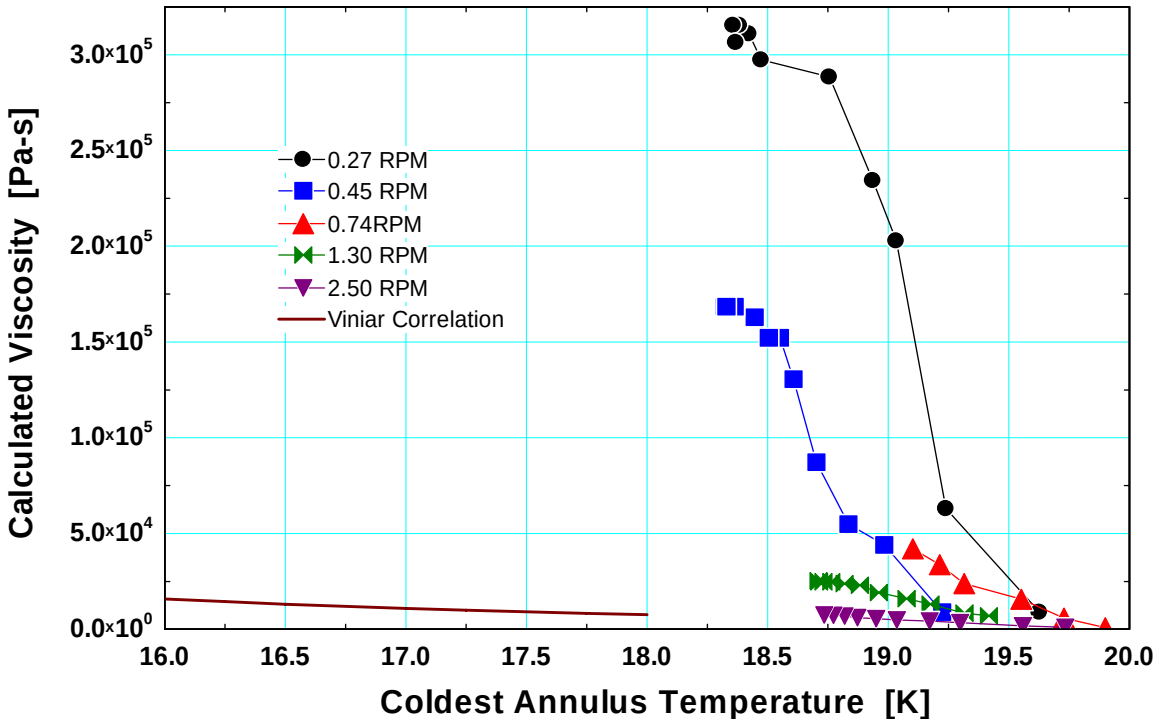

Figure 5.7 Viscosity Results with Viniar Correlation

The values suggest that as the rotation rate increases, the experimental results approach the viscosity values reported by Viniar. At lower rotation rates, the experimental results are much higher, indicating a dynamic shear strength effect.

5.5 Shear Stress Results

Comparing the data in Figure 5.3 with the energy dissipation due to solid sheer forces, given by

$$q_{shear} = A_c \, \sigma_{dyn} \, R \, n \tag{5.2}$$

results in sheer stress values ranging from 0.25 to 1.5 bar, a range comparable to solid hydrogen and solid deuterium values. In equation (5.2), A_c is the contact area between

the material and the chamber, σ_{dyn} is the dynamic shear strength of the solid material, and R is the cylinder radius. No comparable values for solid neon are available in the literature.

In a similar manner, energy dissipation data from Figure 5.4 is used to calculate the shear strength of deuterium shown in Figure 5.8.

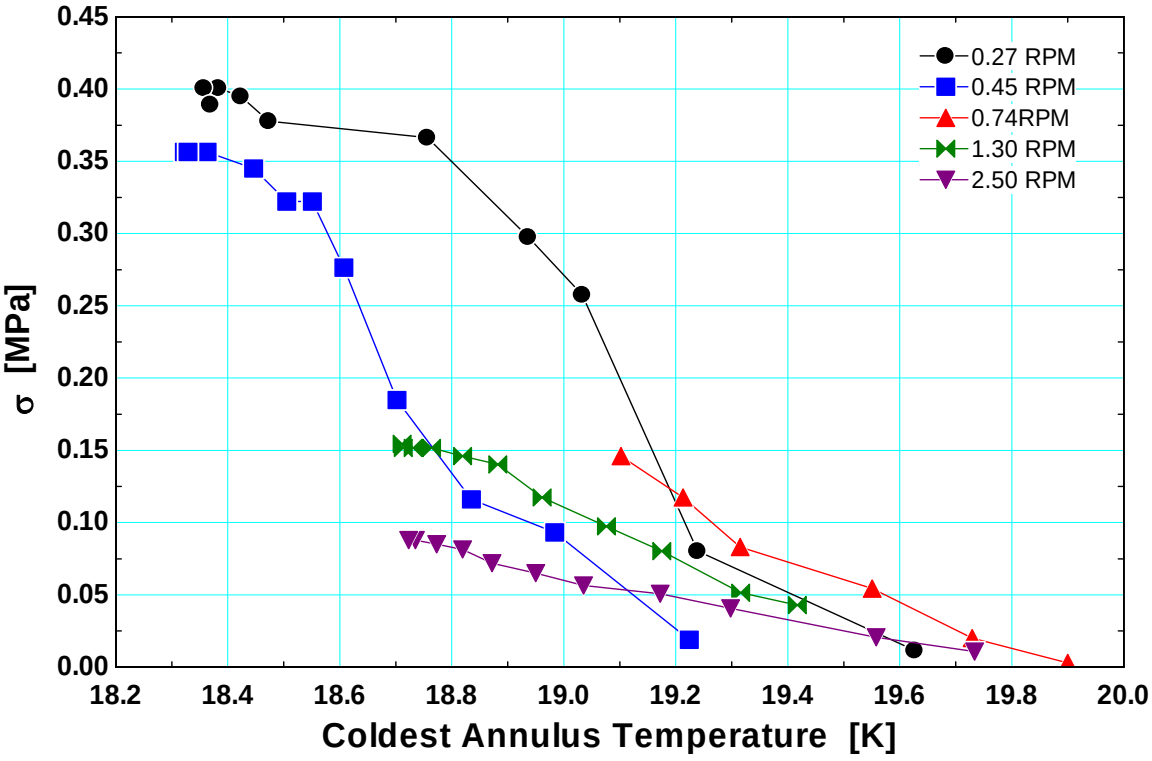

Figure 5.8 Dynamic Shear Strength Results for Multiple Rotation Rates with Deuterium

The dynamic shear strength values are subject to uncertainties in the estimated energy dissipation, shear area, cylinder radius, and rotation rate. Due to the viscous dissipation maintaining the temperatures close to the triple point, coupled with the temperature profile across the annulus, it is likely that the cryogen is not frozen completely around the

annulus. Until a better estimate of the area of frozen cryogen inside the annulus can be obtained, estimation of the uncertainty in the shear is impossible.

The results, compared to shear strength values estimated by Fisher [19], are shown in Figure 5.9.

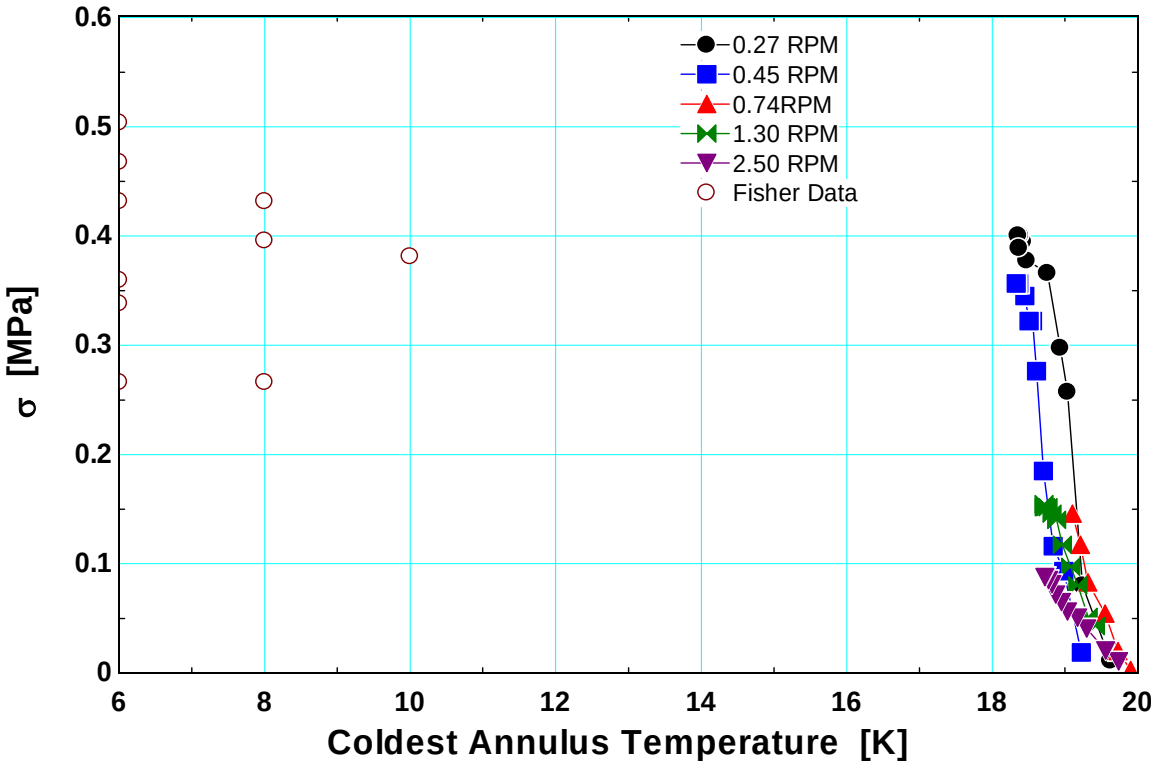

Figure 5.9 Dynamic Shear Strength Results with Fisher Data

The shear strength values reported by Fisher were for temperatures much lower than the energy dissipation experiment experienced. Note that the variance in Fisher's values is similar to that of our own. The temperature difference and variance do not allow a direct comparison with the experimental results; however, the values are of the same order of magnitude.

Future Work

Large uncertainties associated with a couple of the above measurements provide an obvious direction for future measurements of dissipation in frozen cryogens. In particular, the uncertainties in the temperature measurements can be improved through a few relatively simple modifications.

The first modification will enable a better method to determine the temperature profile of the annulus. Rather than relying on temperature profiles generated in the ANSYS® model, temperature sensors will be positioned at the top and bottom on one side of the canister and in the middle of the canister on the opposite side. The modified temperature sensor position and corresponding temperature monitor value is shown in Appendix B.

The heat removal path should also been reconfigured to eliminate two-dimensional temperature gradients. The original thermal plate should be removed and replaced with a thermal link to the bottom center of the canister. This will allow temperature gradients across the annulus to happen in only the vertical direction. In conjunction with the repositioned temperature sensors, the redesigned heat path will allow a better estimation of the amount of solid cryogen under shear.

Repeated measurements with hydrogen, deuterium and neon can be expected to provide a cleaner definition of the dissipation values, viscous and sheer properties, and the associated temperatures. Similar measurements using nitrogen are envisioned with the same cryocooler in the hopes that the average annulus temperature can be brought well

below the cryogen triple point – a feature which was not possible in the tests to date with hydrogen, deuterium, or neon.

Bibliography

1. Energy Information Administration (EIA), *International Energy Annual 2004*, report #:DOE/EIA-0484(2007)

2. Spears B., *ITER*. Website updated December 2007. *http://www.iter.org*

3. *ITER Technical Basis 2002*, ITER EDA Documentation Series No. 24, 2.7.1.5, IAEA Vienna, 2002.

4. Combs S., *Pellet Injection Technology*. Rev. Sci. Instr. 64 (7), 1993.

5. Viniar I., Krasil'nikov S., Skoblikov A., Lukin A., and Saksaganskii G., *A Large Scale Prototype of a Tritium Pellet Injector for the ITER International Tokamak*. Instr. And Exp. Tech. 45 (1), 2002.

6. White J., *Twin Screw Extrusion*. Hanser Publishers, Munich 1991.

7. Andraschko, M. A., *Twin Screw Extrusion and Viscous Dissipation for the Pellet Fueling of Fusion Reactors*, MS thesis, University of Wisconsin - Madison

8. Viniar, I.and Lukin, A. *Screw Extruder Development*, Private Communication from LIRAL International Trading, Inc. St. Petersburg, Russia to Oak Ridge National Laboratory, 1997.

9. Cryogenic Associates Inc., 500 4th Ave. SW, New Prague, MN, United States

10. Latitude Corp., 1003 American Way, Verona, Wisconsin 53593

11. Weisend J G., *Handbook of Cryogenic Engineering*, Routledge,1998

12. R.G. Hansen & Associates, *Table of Thermal Conductivity Integrals*

13. Beer, Johnston, DeWolf, *Mechanics of Materials, McGraw Hill*, 2002

14. Eckels Engineering, *Cryocomp Properties Version 2.0*, 3322 Ebenezer Court Dr., Florence, SC 29501

15. Parker Hanniflin Corp., *Parker O-ring Handbook*, Cleveland, OH 1999-2000

16. Cryomech Inc., *Cryorefrigerator Specifications*., 2001

17. Wisconsin Soldering and Brazing, 5220 N. 125th St., Butler, WI 53007-1103, USA

18. Lakeshore Cryotronics Inc., *Temperature Measurement and Control Catalog*, 2004

19. Fisher P., *Tritium Proof of Principle Pellet Injector*, Oak Ridge National Laboratory, Internal Report ORNL/TM-11781

Appendix A EES Rotameter Conversion Calcuations

```
"choose which fluid you are converting to - in this case deuterium"
fluid$=' deuterium '

"choose which fluid you are converting from- in this case high accuracy air"
fluid2$='air_ha'



"This will determine the density of the rotameter scale fluid, at standard conditions."
rho_from_std=density(fluid2$,T=T_std,P=P_std)
        T_std=convertTemp(C,K,20)
        P_std=1 [atm]*convert(atm,kPa)

"This will determine the density of the fluid that you want to convert the rotameter scale to, at
existing conditions."
rho_gas=density(fluid$,T=T_actual,P=P_actual_absolute)
        T_actual=convertTemp(C,K,24)
        P_actual_absolute=(P_std+P_actual)
        P_actual=17.196[psia]*convert(psia,kPa)

"This is the estimated cooling capacity of the cryocooler at the boiling point of the fluid you wish to
use - in this case for deuterium "
W_dot=4[W]

"This is the latent heat of vaporization of the fluid you wish to use - in this case for deuterium"
lv=302[kJ/kg]*convert(kJ/kg,J/kg)

"This determines the estimated mass flow rate through the rotameter of the fluid you wish to use"
m_dot_to=W_dot/lv

"This determines the estimated volumetric flow rate through the rotameter of the fluid you wish to
use"
m_dot_to=V_dot_CFH_to*rho_gas*convert(ft3/hr,m3/s)

"This is the relationship between volumetric flow of the rotameter scale fluid, and the fluid you
wish to use"
V_dot_CFH_to=V_dot_SCFH_from*sqrt(rho_from_std/rho_gas)

"_____"
"This is how the fluid you wish to use will appear on the scale"
rotameterscale=V_dot_SCFH_from
"_____"
```

Appendix B Temperature Sensor Wiring

Original Wiring Table

Temperature Sensor	Temperature Monitor Pin	Feedthrough Pin	Connection
T1	G	3	I+
	E	4	V+
	H	15	I-
	F	16	V-
T2	J	6	I+
	R	7	V+
	K	18	I-
	S	19	V-
T3	D	9	I+
	B	10	V+
	C	22	I-
	A	23	V-
T4	L	3	I+
	V	4	V+
	M	15	I-
	U	16	V-

218 Temperature Monitor Pin Positions

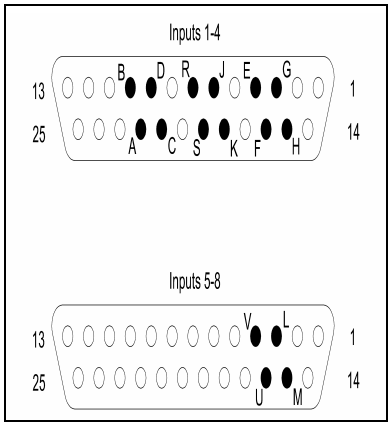

Current Temperature Sensor Location

Temperature Monitor Value	Temperature Sensor Location
T1	Top Back of Canister
T2	Cryocooler 2nd Stage
T3	Mid-height, front of Canister
T4	Bottom Back of Canister

Appendix C Calorimetric Calibration Uncertainty Formulas

Power Uncertainty

$$P = I \cdot V$$

$$\Delta P = \sqrt{\left(\frac{\partial P}{\partial I}\Delta V\right)^2 + \left(\frac{\partial P}{\partial V}\Delta I\right)^2}$$

where

$$\frac{\partial P}{\partial I} = V \ (measured)$$
$$\frac{\partial P}{\partial V} = I \ (measured)$$
$$\Delta I = 0.01 \ [amps]$$
$$\Delta V = 0.01 \ [volts]$$

Annulus Temperature Difference Uncertainty

$$\Delta T_{diff} = \sqrt{(\Delta T_{warm})^2 + (\Delta T_{cold})^2}$$

where

$$\Delta T_{warm} = 0.1 \ [K]$$
$$\Delta T_{cold} = 0.1 \ [K]$$

Appendix D Load Cell Calibration Uncertainty Formulas

Torque Uncertainty

$$T = F\,x$$

$$\Delta T = \sqrt{\left(\frac{\partial T}{\partial F}\Delta F\right)^2 + \left(\frac{\partial T}{\partial x}\Delta x\right)^2}$$

where

$$\frac{\partial T}{\partial F} = x\ (measured)$$
$$\frac{\partial T}{\partial x} = F\ (measured)$$
$$\Delta F = 0.1\ [N]$$
$$\Delta x = 0.001\ [m]$$

Wheatstone Bridge Voltage Uncertainty

$$V = \frac{V_{upper} + V_{lower}}{2}$$

$$\Delta V = \sqrt{\left(\frac{\partial V}{\partial V_{upper}}\Delta V_{upper}\right)^2 + \left(\frac{\partial V}{\partial V_{upper}}\Delta V_{upper}\right)^2}$$

where

$$\frac{\partial V}{\partial V_{upper}} = \frac{1}{2}$$
$$\frac{\partial V}{\partial V_{upper}} = \frac{1}{2}$$
$$\Delta V_{upper} = 10\ [mV]$$
$$\Delta V_{lower} = 10\ [mV]$$

Appendix E Energy Dissipation Uncertainty Formulas

Torque Method

Power Uncertainty

$$P = T\,n$$

$$\Delta P = \sqrt{\left(\frac{\partial P}{\partial T}\Delta n\right)^2 + \left(\frac{\partial P}{\partial n}\Delta T\right)^2 + \Delta V^2}$$

where

$$\frac{\partial P}{\partial T} = n$$

$$\frac{\partial P}{\partial n} = T$$

$\Delta T = torque\ uncertainty$

$\Delta n = rotation\ rate\ uncertainty$

$\Delta V = Wheatstone\ bridge\ voltage\ uncertainty$

Coldest Annulus Temperature Uncertainty

$$\Delta T_{coldest} = \sqrt{(\Delta T3)^2 + (\Delta T_{profile})^2}$$

where

$$\Delta T3 = 0.1\ [K]$$

$$\Delta T_{profile} = 0.5\ [K]$$

Calorimetric Method

Power Uncertainty

$$\Delta P = \sqrt{\left(\Delta P_{calibration}\right)^2 + \left(\Delta T\right)^2}$$

where

$\Delta P_{calibration}$ = *calorimetric calibration uncertainty*
ΔT_{diff} = *annulus temperature difference uncertainty*

Coldest Annulus Temperature Uncertainty

(same as Torque Method)

Appendix F Viscosity Uncertainty Formulas

$$\mu = \frac{q}{\left(\frac{\pi\ D}{h}\right)^2 V}$$

$$\Delta\mu = \sqrt{\left(\frac{\partial\mu}{\partial q}\Delta q\right)^2 + \left(\frac{\partial\mu}{\partial h}\Delta h\right)^2 + \left(\frac{\partial\mu}{\partial D}\Delta D\right)^2 + \left(\frac{\partial\mu}{\partial V}\Delta V\right)^2}$$

where

$$\frac{\partial\mu}{\partial q} = \frac{h^2}{\pi^2 D^2\ V}$$

$$\frac{\partial\mu}{\partial h} = 2\frac{q\ h}{\pi^2 D^2\ V}$$

$$\frac{\partial\mu}{\partial D} = -2\frac{q\ h^2}{\pi^2 D^3\ V}$$

$$\frac{\partial\mu}{\partial V} = -\frac{q\ h^2}{\pi^2 D^3\ V^2}$$

$\Delta q = energy\ dissipation\ uncertainty$

$\Delta h = 0.0005[m]$

$\Delta D = 0.0005[m]$

$\Delta V = 0.0009[m]$